A Spectral Perspective of ~~ENSO Driven~~ the Clear-sky OLR Variability Driven by ENSO

Martina Taddia[1,2], Federico Fabiano[2], Stefano Della Fera[3], Elisa Castelli[2], and Bianca Maria Dinelli[2]

[1]Department of Physics and Astronomy, University of Bologna, via Irnerio 46, 40126, Bologna, Italy
[2]Institute of Atmospheric Sciences and Climate, National Research Council (ISAC-CNR), Via Piero Gobetti, 101, 40129 Bologna, Italy
[3]Institute of Applied Physics, National Research Council (IFAC-CNR), Sesto Fiorentino (FI), Via Madonna del Piano, 10, 50019 Sesto Fiorentino, Firenze, Italy

Correspondence: Martina Taddia (martina.taddia8@unibo.it)

Abstract. The study of short-term unforced variability of the Earth radiative budget can provide much information for the understanding of the long-term effect of external radiative forcing, related to the present climate change. In this regard, inter-annual variability of the Outgoing Longwave Radiation (OLR) is strongly shaped by El-Niño Southern Oscillation (ENSO). So far, the relationship between the OLR and ENSO has been investigated using broadband satellites-based observations, such as those of the Clouds and Earth Radiant Energy System (CERES), finding that the peak of the OLR response lags the peak of ENSO activity. However, such ~~analysis cannot~~ observations cannot directly inform on the individual processes that drive the radiative response to ENSO. Here, we exploit the spectrally-resolved clear-sky OLR fluxes - measured by the Infrared Atmospheric Sounding Interferometer (IASI) and the Atmospheric Infrared Sounder (AIRS) instruments - to expand the observational analysis of ENSO's radiative response~~. The observed signal is then decomposed using a spectral kernel analysis into~~ , showing that its intensity and lag vary along the spectral dimension. The spectral fingerprint of water vapor, surface and air temperature, and ozone feedback ~~,~~ is then calculated using a set of spectral kernels to evaluate the role of individual processes in building the overall response. Results show a strong contribution coming from the ozone absorption band, along with a contribution of opposite sign coming from the the core of the carbon dioxide band, which is mainly affected by stratospheric temperature. This analysis confirms the important role of the spectral dimension to study climate processes. In this regard, it sets the basis for a spectral diagnostic to evaluate how ENSO driven variability is reproduced by climate models.

1 Introduction

The Outgoing Longwave Radiation (OLR) ~~is~~ encompasses the energy flux ($\mathrm{Wm^{-2}}$) emitted by the Earth towards space across the ~~thermal and far infrared (FIR)~~ far and thermal infrared spectral regions (from 100 to about 3330 ~~$\mathrm{cm^{-1}}$, 3-100 μm~~$\mathrm{cm^{-1}}$) and represents the main mechanism by which the climate system loses energy to maintain its ~~equilibrium. It contains both the signature of the increased concentration of radiatively active species - such as carbon dioxide~~ thermal equilibrium. The long-term trend of the OLR bears the signal related to the increase of carbon dioxide concentration and other Greenhouse

Gases (GHGs), driving the present-day climate change~~ and~~, as well as that of the system's radiative response, produced by the warming of the planet's surface and resulting climate feedbacks.

To monitor the changes in OLR emission through time we can rely on satellite measurements of the top-of-atmosphere (TOA) OLR. One of the most important instruments is the Clouds and Earth Radiant Energy System (CERES). It has flown since 2000 on board the Terra and Aqua platforms and it has now achieved more than 20 years of stable records of the Earth energy budget and its components. Despite that, the available observational records are not yet long enough to accurately quantify the long-term trend of the OLR and use it to constrain climate models feedbacks (Uribe et al., 2024). The exact magnitude of climate feedbacks, which determine the ultimate warming of the planet in response to forcing, is still uncertain and global climate models (GCMs) struggle to agree on a precise value. For example, a stronger positive ~~clouds feedback in Coupled Models~~ cloud feedback in the Coupled Model Intercomparison Project phase 6 (CMIP6) is the cause of a higher Effective Climate Sensitivity (ECS) estimate, with values between 1.8 - 5.6 K, exceeding the range 2.1 - 4.7 K, obtained with the previous generation of models (CMIP5) (Zelinka et al., 2020). ~~On the other hand, several satellite instruments have been deployed to measure the OLR from space, but the available observational record is not yet long enough to accurately quantify the long-term trend and use it to constraint climate models feedbacks (Uribe et al., 2024).~~ A possible way ahead is represented by the study of the planet's internal variability from observations. The OLR is in fact also subjected to fluctuations on seasonal and interannual timescales~~and several~~. Several research efforts have been focused on the study of the short-term variability to improve the understanding of feedback processes on longer timescales (Dessler et al., 2008; Dessler, 2010, 2013; Uribe et al., 2022).

On the inter-annual time scale, El-Niño Southern Oscillation (ENSO) is the dominant variability mode of the climate system. It causes changes in the Tropical Pacific Sea Surface Temperature (SST) coupled with changes in the above atmospheric circulation, affecting the Earth's climate on a global scale (McPhaden et al., 2020). ENSO induced perturbations to atmospheric and surface variables strongly affect the ~~Top-Of-Atmosphere (TOA) OLR. As shown by~~ TOA OLR. Loeb et al. (2012) and Susskind et al. (2012) ~~,~~ studied the effect of ENSO ~~is detectable in the OLR measured by the Clouds and Earth Radiant Energy System (CERES), which~~ on the OLR using the first decade of measurements acquired by the CERES instrument. They both show that the OLR co-varies significantly with ENSO activity, assuming positive (negative) anomalies in correspondence to El-Niño (La-Niña) phase. The main radiative feedback driven by ENSO induced SST perturbations involves water vapor, temperature and clouds properties changes (Huang et al., 2021). Their evolution during the ENSO life cycle provides information on the feedbacks important for ENSO developing and maintenance. Particularly, the atmosphere exerts an overall positive feedback that act to strengthen ENSO during its developing phase (Kolly and Huang, 2018; Huang et al., 2021). This result is also confirmed by Ceppi and Fueglistaler (2021), ~~who use broadband measurements~~ which used measurements of broadband energy fluxes to investigate the time relationship between the net TOA Earth Radiative Budget and ENSO. ~~Ceppi and Fueglistaler (2021) show that the SST pattern effect (Stevens et al., 2016) is responsible for the out-of-phase relationship between the radiative response and SST anomalies, with the first leading the ENSO peak, thus suggesting a two-way coupling between the atmosphere and ocean.~~

~~The study of the radiative response to ENSO potentially allows to better constrain climate feedbacks and evaluate climate model performance, inspecting their representation of the coupled atmosphere-ocean dynamics (Andrews et al., 2015; Armour et al., 2024; . Indeed, there are evidences that the radiative response to ENSO is still not completely reproduced in both its amplitude and timing (Kolly and Huang, 2018; Planton et al., 2021; Ceppi and Fueglistaler, 2021). While the SST pattern effect plays an important role for the relationship between unforced and forced feedbacks that can be used as an emergent constraint for climate models (Davis et al., 2024; Rugenstein et al., 2025). Hanke and Proistosescu (2024) propose ENSO as an emergent constraint on the pattern effect.~~

~~The present work aims to demonstrate the value of the spectral dimension in OLR measurements for the understanding of the mechanisms that drive the radiative response to ENSO. So far, OLR variability driven by ENSO has been examined~~ All the works presented above examined ENSO driven variability using broadband OLR observations, which provide the total ~~radiance~~ radiative flux integrated over the IR spectral range (e.g. 50 - 2000 cm^{-1} for CERES). ~~The main advantage of the spectral dimension is the possibility to isolate single contributions by examining different spectral regions and to identify the atmospheric layers where the radiation originates (Brindley and Bantges, 2016). The~~ However, we can also rely on spectral OLR measurements (the integrand of the broadband radiance), which has consolidated since the beginning of this century thanks to the availability of instruments such as the Atmospheric Infrared Sounder (AIRS), the Infrared Atmospheric Sounding Interferometer (IASI) or the Cross-track Infrared Sounder (CrIS) (Brindley and Bantges, 2016). For instance, Huang and Ramaswamy (200 investigated the OLR variability in relation to SST using spectral measurements acquired by the AIRS instrument and the analysis of the trend of the first ten years of observations ~~acquired by the Infrared Atmospheric Sounding Interferometer (IASI), shows~~ of IASI (from 2008 to 2017) revealed the spectral signature related to both the increase in GHGs concentration ~~, such as carbon dioxide and methane, and the signal related~~ and to ENSO variability across channels sensitive to water vapor and temperature (Whitburn et al., 2021). Using IASI observations, Roemer et al. (2023) calculated the ~~LW~~ net longwave (LW) spectral feedback parameter and directly observed the spectral fingerprint due to changes in relative humidity for an increasing value of global mean surface temperature. ~~Moreover~~

In addition, spectral OLR have been proven to be a powerful method to assess climate model ~~performances~~ performance, allowing to reveal biases otherwise hidden by ~~compensation~~ compensating effects when broadband fluxes are considered (Della Fera et al., 2023; Huang et al., 2007; Leroy et al., 2008; Huang et al., 2014). The study of the spectral radiative response to ENSO potentially allows to better constrain climate feedbacks and evaluate the performance of climate models, inspecting their representation of the coupled atmosphere-ocean dynamics (Andrews et al., 2015; Armour et al., 2024; Andrews et al., 2022) . Indeed, there is evidence that the radiative response to ENSO is still not completely reproduced in both its amplitude and timing by climate models (Kolly and Huang, 2018; Planton et al., 2021; Ceppi and Fueglistaler, 2021).

The present work aims to demonstrate the value of the spectral dimension in OLR measurements for the understanding of the mechanisms that drive the radiative response to ENSO. Building on the analysis by Ceppi and Fueglistaler (2021), we first assess the OLR response to ENSO using CERES broadband observations. We then explore the ~~potentiality~~ potential of the spectral dimension to identify ~~which processes~~ the processes that drive the timing and the magnitude of the OLR anomalies, comparing measurements acquired by ~~two hyperspectral sounders, the Infrared Atmospheric Sounding Interferometer (IASI~~

~~) and the Atmospheric Infrared Sounder (AIRS)~~IASI and AIRS instruments. Finally, the role of water vapor, surface and air temperature spectral feedback is investigated, calculating their radiative changes by means of spectral radiative kernels. ~~We develop a new diagnostics that~~ Our analysis highlights the role of different feedback processes ~~, and~~ in driving OLR variability and we propose to apply it for a stricter evaluation of climate model performance.

The article is organized as follows: a description of the datasets and of the methodology applied is provided in section 2; the results of the analysis are presented in section 3; the main findings are discussed in section 4, and final conclusions are drown in section 5.

2 Data and Methods

~~The analysis uses~~

2.1 Observational datasets

The analysis is based on monthly mean OLR spectral fluxes in clear-sky conditions derived from ~~CERES, AIRS and IASI observations.~~ spectral radiances acquired by the AIRS and IASI instruments.

~~CERES~~

AIRS is a grating array spectrometer that measures spectrally resolved radiances across three different bands, 650-1136 cm^{-1}, 1216-1613 cm^{-1}, 2170-2674 cm^{-1} (Aumann et al., 2003). OLR spectral fluxes have been derived for both clear and all-sky conditions by Huang et al. (2008), using measurements acquired by the instrument flying on board the Aqua satellite from November 2002 to present days. Simulated radiances have been used to fill the spectral gaps and extend the original spectral range below 650 cm^{-1}, down to 15 cm^{-1}. The final product consists of monthly mean spectral fluxes computed at 10 cm^{-1} from 15 to 1995 cm^{-1}, with a horizontal resolution of 2° latitude by 2° longitude. Two separate flux products are provided for the two AIRS overpass times at the equator, 01:30 and 13:30 local time (LT). In this study, we use the average of these two overpasses.

IASI is a Fourier transform spectrometer which measures radiances across the range from 645 to 2760 cm^{-1}, with a spectral resolution of 0.25 cm^{-1} (Simeoni et al., 2004). Whitburn et al. (2020) retrieved spectral fluxes from spectrally resolved radiances in clear-sky conditions, acquired by the instruments flying on board the MetOp-A (10/2007-12/2021), B (2013-) and C (2017-) platforms. For this study, we selected fluxes derived from measurements acquired by IASI on board the MetOp-A, since it ensures the greatest temporal overlap with the AIRS and CERES datasets. The dataset consists of monthly mean spectral fluxes for the period from January 2008 to October 2021. Spectral fluxes are provided over a 2° longitude by 2° latitude grid and span the wavenumber range from 645 to 2300 cm^{-1}, with a spectral resolution of 0.25 cm^{-1}. Two products are provided for night-time (21:30 LT at the equator) and daytime (09:30 LT at the equator) observations, respectively. As was as done for AIRS, these overpasses have been averaged. It should be noted that the MetOp-A platform began drifting from its nominal orbit in autumn 2017, resulting in an earlier local time of the ascending node.

Table 1. Main features of the datasets used.

	CERES	AIRS	IASI
Temporal Resolution	monthly	monthly	monthly
Temporal Coverage	01/2000-12/2020	09/2002-12/2021	01/2008-10/2021
Horizontal Resolution	1°x1°	2°x2°	2°x2°
Spectral Coverage (~~cm^{-1}~~cm^{-1})	50-2000	15-1995	645-2300
Reference	*Loeb et al. (2020)*	*Huang et al. (2008)*	*Whitburn et al. (2020)*

In addition to AIRS and IASI spectral fluxes, we used broadband OLR values derived from CERES measurements. CERES is a broadband radiometer ~~(Wielicki et al., 1996)~~ with three channels that measure radiances across the whole spectrum (~~0.3-200 μm~~50-3000 cm^{-1}), the shortwave (SW, ~~0.3-5 μm~~2000-3000 cm^{-1}) and the atmospheric window (~~8-12 μm) regionsrespectively~~830-1250 cm^{-1}) regions, respectively (Wielicki et al., 1996). We use the CERES ~~energy balanced and filled~~ Energy Balanced and Filled (EBAF) ~~edition~~ Edition 4.1 data product (Loeb et al., 2020), which gathers data collected by different CERES instruments on board Terra and Aqua platforms since ~~2000 (data collection is still ongoing).~~ 2000. Two clear-sky products are available, one that only considers cloud-free observations and another that additionally applies a correction factor for a better comparison with climate models output, for which clear-sky fluxes are artificially produced by removing clouds from the flux calculation. ~~For this work the~~ The first product has been selected ~~,~~ for consistency with IASI and AIRS observations. CERES-EBAF 4.1 provides monthly mean TOA OLR fluxes with an horizontal resolution of 1° ~~x~~ per 1° and a temporal coverage from January 2000 to March 2022.

~~AIRS is a grating array spectrometer that has flown on board Aqua satellite since 2002 (Aumann et al., 2003). It covers three different bands, 650-1136 cm^{-1}, 1216-1613 cm^{-1}, 2170-2674 cm^{-1}. Monthly mean OLR spectral fluxes have been derived by Huang et al. (2008, 2019) for both clear and all-sky conditions. AIRS fluxes are calculated exploiting the same angular distribution models of CERES, for this reason the computation has been performed only for AIRS pixel that overlap up to a certain threshold with CERES ones. In the clear-sky scenario only clear-sky CERES observations are considered affecting the final AIRS spatial sampling. The original spectral range has been filled with simulations and extended to the FIR spectral region (100-600 cm^{-1}), so that the final product consists of monthly mean spectral fluxes computed every 10 cm^{-1} from 15 to 1995 cm^{-1}. AIRS data range from November 2002 to December 2021, with a horizontal resolution of 2° x 2°.~~

~~IASI is a Michelson interferometer which measures radiances across the 645-2760 cm^{-1} spectral range with a resolution of 0.25 cm^{-1} (Simeoni et al., 2004). It has flown on board MetOp-A (10/2007-12/2021) satellite and it is currently operating on board the MetOp-B (2013-) and C (2013-). We use the monthly climatology developed by Whitburn et al. (2020); Whitburn (2021b) using observations collected by IASI instrument on board the MetOp-A, which has the longest temporal coverage, from January 2008 to October 2021. Spectral fluxes are provided from 645 up to 2300 cm^{-1} (to avoid contamination of shortwave radiances) keeping the original resolution of 0.25 cm^{-1} and for only clear-sky scenario. They have an horizontal resolution of 2° per 2° latitude. The~~ The main features of the three datasets are resumed in Table 1.

~~All the datasets have been regridded to a common grid of 2.5° latitude per 2.5° longitude, through a bilinear interpolation. We focused on the tropical zone (30°S-30°N), where the radiative perturbations induced by ENSO are strongest, and on values above ocean, to avoid introducing biases in the comparison of non-simultaneous measurements, which can arise from the rapid temperature variability typical of land surfaces (Huang and Yung, 2005; Whitburn et al., 2021). The period from 01/2008 to 12/2020, common to all the observational datasets, has been selected for the analysis. We computed monthly anomalies removing the seasonal cycle and the linear trend for the whole period.~~

~~As a measure of the ENSO phase over the considered period, we use the Niño 3.4 index. Following Trenberth (1997), deseasonalized and detrended SST anomalies have been calculated for the Niño 3.4 region (5°S-5°N,170°-120°W), and then smoothed with a 5-months running mean. Area averaged SST are provided by the NOAA-PSL database () to calculate the Niño 3.4 index.~~

~~We use lagged regressions to investigate the time relationship between the OLR and ENSO. Specifically, radiative anomalies have been regressed onto the Niño 3.4 index shifted one month at a time from -12 to +12 month (25 slopes are obtained at the end of the procedure). The 95% statistical significance of the slopes has been assessed with a two-tailed t-test. The regression coefficients are a measure of the radiative perturbations driven by ENSO induced SST anomalies, to which we will refer to as "ENSO feedback" during the rest of the paper, as done also by Kolly and Huang (2018); Huang et al. (2021).~~

2.2 Spectral Radiative Kernels

~~To disentangle the contributions of atmospheric temperature, water vapor, ozone and surface temperature to the change in the radiative fluxes driven by ENSO, we apply a spectral kernel analysis.~~ Radiative kernels (or Jacobians) represent the partial derivative of spectral flux or radiance with respect to specific climate variables~~(temperature, surface temperature, water vapor and ozone),~~ , evaluated across the atmospheric levels~~in~~ . They can be used to estimate the OLR perturbation at the TOA resulting from changes in atmospheric and surface climate variables.

For this study we use a set of clear-sky ~~conditions. These derivatives are~~ spectral kernels developed by Della Fera et al. (2025) . The kernels have been computed using the ~~Radiative Transfer for TOVS (RTTOV v13) model (Matricardi, 2009) , based on~~ RTTOV model (Radiative Transfer model for the TIROS-N Operational Vertical Sounder) (Matricardi, 2009) and monthly mean profiles from the ~~ECMWF~~ European Center for Medium-Range Weather Forecast (ECMWF) Reanalysis v5 (ERA5) dataset ~~for the~~ as the input for meteorological fields. The derivatives have been computed for three different years 2008, 2009, and 2010, and then averaged to obtain representative monthly kernels ~~. As done by Huang et al. (2014), at least one year of data is sufficient for kernels computation.~~

~~The RTTOV model is customized to reproduce the synthetic radiance of specific instruments working in different spectral ranges, from visible to microwaves. In our case, since we aim to compute the derivative across the entire Earth infrared spectral range from 100 to 2300 cm^{-1}, we calculated the derivative of synthetic radiance for FORUM (the EE-9 selected by ESA, Far-Infrared Outgoing Radiation Understanding and Monitoring) in the FIR spectral region (100–650 cm^{-1}), using its associated instrumental function, as well as that of IASI in the MIR spectral range (650–2300 cm^{-1})~~of surface and atmospheric temperature, water vapor and ozone. Furthermore, in order to obtain the derivatives of the spectral flux (~~W m^{-2}~~

~~$(\mathrm{cm}^{-1})^{-1}$~~ $\mathrm{W/m^2/cm^{-1}}$), radiance derivatives (~~$\mathrm{W}\ m^{-2}(cm^{-1})^{-1}\ \mathrm{sr}^{-1}$~~ $\mathrm{W/m^2/cm^{-1}}$/sr) were computed at three distinct viewing angles (24.29°, 53.80°, 77.74°). The resulting values were then integrated using Gaussian quadrature, which has been shown to yield accurate results for clear-sky radiative transfer calculations (Clough et al., 1992). ~~The resulting dataset~~ More details regarding the construction of the spectral kernels can be found in Della Fera et al. (2025).

The resulting product consists of radiative kernels, averaged over 10 ~~cm^{-1}~~ cm^{-1} intervals, from 100 to 2300 ~~cm^{-1}~~ cm^{-1}, spanning 17 pressure levels (hPa): 1000, 925, 850, 700, 600, 500, 400, 300, 250, 200, 150, 100, 70, 50, 30, 20, 10, on a horizontal grid of 2.5° ~~×~~ per 2.5°.

The ~~perturbation to~~ change in the radiative flux associated to the change in each climate variable is obtained multiplying the respective radiative kernel by the anomaly of ~~the variable of interest~~ that variable and then, for 3D ~~variables~~fields, summing over the pressure levels to obtain the total atmospheric response.

~~Atmospheric variables~~ Surface and atmospheric temperature, water vapor and ozone fields are taken from the monthly ECMWF ERA5 reanalysis (Hersbach et al., 2023b)~~,~~. Atmospheric variables are selected on the same 17 pressure levels used for the radiative kernels ~~. We consider the period~~ computation. The anomalies are computed relative to the mean for the period selected for the analysis, from January 2008 ~~–~~to December 2020.

2.3 Lagged regression analysis

The time relationship between OLR anomalies and ENSO activity has been investigated through a lagged regression analysis. The period from January 2008 to December 2020, ~~and compute the anomalies~~ which is common to all the observational datasets has been chosen.

All the datasets have been regridded to a common grid of 2.5° latitude per 2.5° longitude, through a bilinear interpolation. Then, the monthly OLR anomaly has been calculated by subtracting the monthly climatology, relative to the ~~mean over the entire time span.~~

3 ~~Results~~

~~We present here the main results of the analysis, starting from the broadband fluxes and then moving to the spectral dimension~~period from January 2008 to December 2020, from the OLR time series. In addition, the monthly OLR anomalies have been detrended by subtracting the linear trend, in order to isolate the internal variability from the signal of increased GHG concentrations over the given period.

2.1 ~~Broadband radiative response to ENSO~~

~~The slopes of the lagged regressions between the OLR anomalies~~ The Niño 3.4 index has been used as a measure of ENSO phase and magnitude. It is defined as the average SST anomaly over the Niño 3.4 region (5°S-5°N, 170°-120°W), smoothed with a five-month running mean (Trenberth, 1997). Area-average SSTs provided by the NOAA-PSL database have been used for its calculation (https://climatedataguide.ucar.edu/climate-data/nino-sst-indices-nino-12-3-34-4-oni-and-tni). The resulting Niño 3.4 index is plotted in Figure 1.

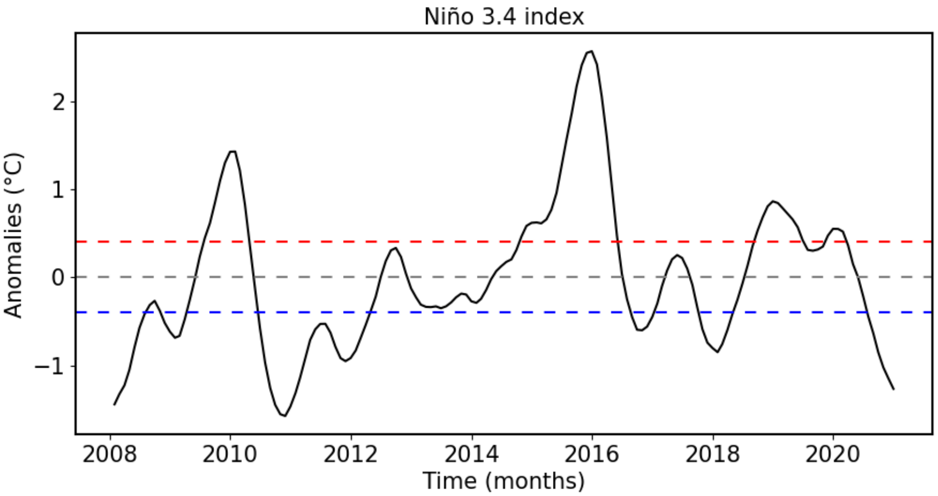

Figure 1. The Niño 3.4 from January 2008 to December 2020 calculated using the area averaged SST provided by the NOAA-PSL database. The blue (red) horizontal line marks the -0.4 (0.4) °C temperature anomalies, above which ENSO episodes are classified as La-Niña (El-Niño).

Lagged regressions have been calculated performing a linear regression between the radiative anomaly and the Niño 3.4 index ~~performed for broadband fluxes are reported in Figure 2 as a function of lags. The sign of the OLR is defined as positive upward, meaning that for positive slopes an increase in OLR emission takes place,~~ as follow:

$$y = m \cdot x + q \tag{1}$$

In equation 1, y and ~~vice versa for negative. For both AIRS and IASI,~~ x are the OLR anomaly and Niño 3.4 index time series, respectively, from January 2008 to December 2020; the variable x has been shifted one month at a time from -12 to +12 months, resulting in 25 regression coefficients, m, being obtained at the end of the procedure. The regression coefficients, (units of $\mathrm{W/m^2/K}$), are a measure of the radiative perturbations driven by ENSO induced SST anomalies, which we will refer to as "ENSO feedback" in the rest of the paper, as done also by Kolly and Huang (2018) and Huang et al. (2021). The 95% statistical significance of the regression coefficients has been assessed with a two-tailed t-test.

The analysis focused on the tropical zone (30° S - 30° N), where the radiative perturbations induced by ENSO are strongest, and on values above ocean, to avoid introducing biases in the comparison of non-simultaneous measurements, which can arise from the rapid temperature variability typical of land surfaces (Huang and Yung, 2005; Whitburn et al., 2021).

3 Results

Here, we present the main results of the analysis, starting from the broadband fluxes and then moving to the ~~radiative fluxes have been integrated along the~~ spectral dimension.

3.1 Broadband radiative response to ENSO

The OLR response to ENSO variability is presented first from a broadband perspective. In the case of AIRS, ~~two broadband fluxes have been calculated: one using spectral channels~~ the spectral fluxes are integrated over two different spectral ranges: from 50-1995 ~~cm^{-1} (dashed line)~~ cm^{-1}, to be as consistent as possible with CERES~~(encompassed~~, which encompasses the range from 50 to 2000 ~~cm^{-1}), and a second limited to the IASI spectral range (~~cm^{-1}, and from 645-1995 ~~cm^{-1}). For both the two spectral range encompassed, the magnitude of the slopes increases moving from negative to positive lags and reaches a maximum at~~ cm^{-1}, to match the spectral range encompassed by IASI. Figure 2 shows the tropical mean broadband OLR response to ENSO as a function of the time lag obtained using fluxes from CERES, IASI and AIRS. Note that, in order to be consistent with the definition of climate feedbacks, the sign of the OLR response has been inverted. Thus, a negative ENSO feedback corresponds to an enhanced OLR emission at the TOA, conversely, a positive feedback is associated with a decrease in OLR.

The radiative response depicted in Figure 2 suggests an increase in OLR emission at the TOA associated to ENSO. In more detail, the total LW ENSO feedback becomes negative starting from about five months ahead of ENSO peak. The negative peak is reached at a lag of 2 months, ~~showing that ENSO is associated to an increase in~~ and the response gradually weakens thereafter. This result agrees with Ceppi and Fueglistaler (2021), who found a similar OLR response to ENSO in clear-sky conditions, suggesting that it is likely driven by the Planck effect.

When the ~~TOA OLR emission. When both the MIR (650–2300 cm^{-1}) and the FIR spectral region (100–650 cm^{-1}) are~~ entire spectral region from 50 to 2000 cm^{-1} is accounted for, the ~~maximum slope is of 0.46~~ OLR peak at the 2-months lag is of -0.46 $\pm$ 0.11 ~~Wm^{-2}K^{-1}~~ Wm^{-2}K^{-1} for AIRS and ~~0.46~~ -0.46 $\pm$ 0.12 ~~Wm^{-2}K^{-1}~~ Wm^{-2}K^{-1} for CERES, ~~while its value is of 0.31~~ whereas it decreases to -0.31 $\pm$ 0.05 ~~Wm^{-2}K^{-1}~~ Wm^{-2}K^{-1} for AIRS and ~~0.31~~ -0.31 $\pm$ 0.05 ~~Wm^{-2}K^{-1}~~ Wm^{-2}K^{-1} for IASI, when ~~only the MIR~~ the 645-1995 cm^{-1} wavenumber range is considered. ~~This denotes that an important part of~~ These values denote that approximately 30% of the total OLR emission during ENSO is achieved ~~across the FIR, confirming its importance~~ between 50 and 645 cm^{-1}, confirming the importance of the Far-Infrared (FIR) spectral region (100-600 cm^{-1}) for the TOA Earth Radiative Budget ~~(ERB).~~ (Palchetti et al., 2020; Harries et al., 2008).

Although we find an excellent agreement in the ~~value of the maximum slope~~ magnitude of the OLR response peak between CERES and AIRS, ~~there is a slight delay in~~ the AIRS signal ~~, with the peak delayed by 1 month(at 3-month lag)~~ exhibits a delay of one month, peaking at 3-months lag, and a smaller ~~slope~~ value at negative lags~~. The difference is likely due to AIRS's clear-sky scene selection, as will be investigated further in Section 4. The~~, compared to CERES. Instead, the agreement between AIRS and IASI is excellent, with minor differences at negative lags.

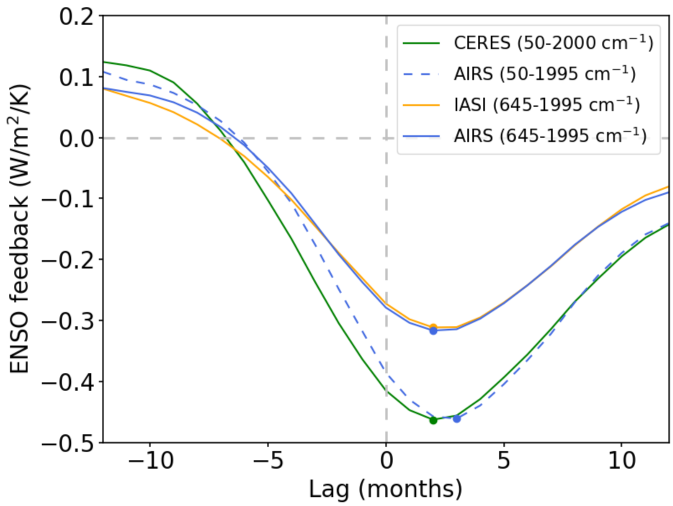

Figure 2. Lagged regressions of the tropical mean ~~integrated~~ broadband OLR anomalies from CERES (green), AIRS (blue) and IASI (orange), respect to the Niño 3.4 index, from lag -12 to +12 months. The sign of the OLR has been inverted (negative feedback = positive OLR anomaly).

3.2 ENSO spectral footprint from AIRS and IASI

~~We now wish~~ In order to examine the factors ~~controlling~~ that control the magnitude and timing of the ~~response peak. To do so, the analysis has been extended~~ clear-sky ENSO longwave feedback, we have extended the analysis to the spectral dimension~~and lagged regressions~~. Lagged regressions between the tropical mean OLR anomalies and the Niño 3.4 index have been performed ~~for each spectral channel of~~ at each wavenumber encompassed by IASI and AIRS ~~. To allow for a~~ spectral fluxes. To enable direct comparison, IASI ~~has been resampled at~~ spectra have been resampled to the same resolution ~~of AIRS~~ as the AIRS dataset (10 ~~cm^{-1}).~~

~~The maps in the central and bottom panels of Figure 3 show the regression slopes (unit of Wm^{-2}K^{-1}) obtained~~ cm^{-1}). Figure 3 shows the spectral ENSO feedback as a function of ~~wavenumber and lag for IASI and AIRS. The top panel shows the slopes as a function of wavenumber alone for 2-month lag~~ wavenumbers and time lag (panels a and b), and for a time lag of two months (panel c), where the broadband ~~regression slopes peak~~response peaks.

~~The first thing to note is that a different response is obtained at different wavenumbers, which are associated to~~ Different responses are obtained across the spectrum. Specifically, different spectral regions are associated with a characteristic lag, as well as a particular sign and magnitude ~~. A positive peak is found between 1000 - 1065 cm^{-1}, at 3-month lag, where the ozone absorption band, centered at 1043 cm^{-1}, is located. This constitutes the response with the highest magnitude across the whole spectrum. Other important contributions come from the~~ of the ENSO feedback. The wings of the carbon dioxide absorption band ($\sim$ 600-645 ~~cm^{-1}~~ cm^{-1} and $\sim$ 700-800 ~~cm^{-1}), associated to positive slopes with a lag of 3-month, and from its center ($\sim$ 645-700 cm^{-1}), characterized by negative slopes at 5-month lag. The two~~ cm^{-1}), the atmospheric windows ($\sim$ 800-1000

~~cm^{-1} and~~ cm^{-1} and $\sim$ 1100-1200 ~~cm^{-1}) show both positive slopes centered at lag equal to +2 months~~cm^{-1}) and the ozone absorption band ($\sim$ 1000 - 1065 cm^{-1}) are all associated with a negative ENSO feedback. Below 600 ~~cm^{-1} we can relay only on~~ cm^{-1}, where only AIRS simulated spectral fluxes ~~. These wavenumbers exhibit positive slopes, too, of higher magnitude between~~ are available, a widespread negative ENSO feedback emerges. The only positive feedback comes from the center of the carbon dioxide absorption band ($\sim$ ~~400-600 cm^{-1}, than between $\sim$ 100-400 cm^{-1}. These two spectral regions also differ in the time~~ 645-700 cm^{-1}).

The strongest response across the whole spectrum is found in correspondence with the ozone absorption band, where the OLR is sensitive mainly to surface temperature and upper tropospheric/lower stratospheric ozone. It is followed by the carbon dioxide band, wings and center, which provide information on the tropospheric and stratospheric temperature, respectively, and the atmospheric windows, where radiation is mainly sensitive to the surface temperature. Finally, the negative response in the FIR is likely driven by water vapor, which exhibits strong absorption in this spectral range (Harries et al. (2008)).

The time lag of the ENSO feedback is also spectrally dependent. This is highlighted by thicker black dots in Figure 3, which mark the lag of the ENSO feedback peak at each wavenumber. A lag of ~~the response, centered at 3-month lag for the first and at 2-month lag for the second.~~ 2 months is observed across the atmospheric windows, while a 3-months lag characterizes the spectral regions associated with the wings of the carbon dioxide and the ozone absorption band. Finally, at the center of the carbon dioxide band the OLR response peaks at a lag of 5 months.

~~Spectral footprints for~~ A summary of the ENSO spectral feedback for the spectral regions discussed above is provided by Table 2. It reports the value of the ENSO feedback integrated over each wavenumber interval, along with the lag at which the OLR response peaks.

AIRS and IASI spectral footprints are generally in a good agreement, showing the same main features. ~~Nevertheless, there~~ There are some differences in the magnitude of the ~~slopes in~~ response peak within the atmospheric window ~~between~~ ($\sim$ 800-1000 ~~cm^{-1} and within the ozone absorption band. AIRS slopes within the atmospheric window are higher than IASI, while they are lower~~ cm^{-1}), where the AIRS signal is slightly higher than that of IASI (Table 2, fifth row), but inside the uncertainty range. The opposite behavior is observed within the ozone absorption band ~~. Since~~ (Table 2, sixth row). One factor to consider is the difference in overpass times between AIRS and IASI~~differs only in these two spectral regions, the opposite biases could compensate each other when broadband fluxes are calculated giving an almost perfect agreement obtained with broadband lagged regressions (see Figure 2). As for regards the origin for these discrepancies, an important factor that must be considered is~~ . This could partly explain the observed bias within the atmospheric window, where radiance is more sensitive to surface temperature (Whitburn et al., 2020). However, the different clear-sky scene selection ~~(see section section 2). The more conservative approach used for AIRS could explain the higher slopes within the atmospheric window. However, these particular aspects will be further discussed~~ could also play a role. Specifically, AIRS clear-sky fluxes are based on the collocated CERES measurements considered as clear-sky by the scene type information provided by the Moderate Resolution Imaging Spectroradiometer (MODIS), as described in Huang et al. (2008). We found that this strategy produced a more conservative cloud screening than that of IASI (not shown). This aspect will be more evident in Section 3.4, when we will examine the spatial pattern of the ~~LW response is examined~~ENSO feedbacks.

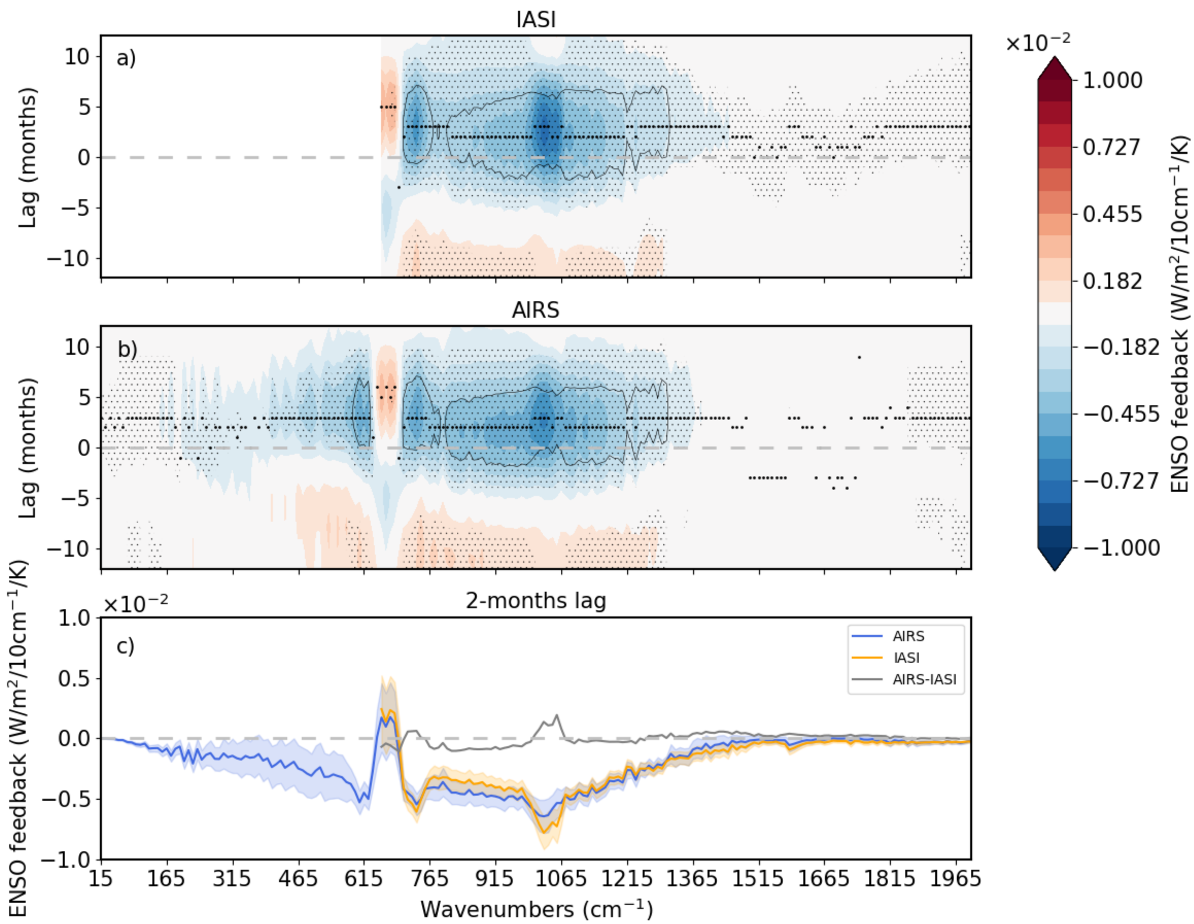

Figure 3. ~~Slopes~~ a) Lagged regressions of the ~~lagged regressions between~~ tropical mean spectral OLR anomalies ~~and~~ from IASI respect to the Niño 3.4 index as a function of ~~wavenumber at a fixed~~ wavenumbers and lag~~of 2 months (top panel~~. b) ~~, and~~ Same as a~~function~~ , but for AIRS. c) Regression of ~~wavenumber and lags~~ the spectral OLR anomalies respect to the Niño 3.4 index at the 2-months lag for AIRS (blue) and IASI (~~central panel~~orange), and ~~AIRS~~ their difference (~~bottom panel~~gray). ~~Shades envelope the 95% confidence interval. Thinner~~ In panels a and b, thinner black dots mark 95% significance of the slopes, while thicker black dots mark the lag where the ~~slope peaks~~ strongest radiative response occurs at each wavenumber. Contour lines mark correlation values of 0.5. In panel c, shades envelope the 95% confidence interval. As above, the sign of the OLR has been inverted (negative feedback = positive OLR anomaly).

Table 2. The total ENSO feedback in different spectral regions obtained from AIRS, IASI and from the reconstruction using spectral radiative kernels. The values reported correspond to the integral over the selected wavenumber intervals at the lag of the radiative response peak. The associated confidence interval (95%) is reported.

Wavenumber range (cm^{-1})	Lag (Months)	ENSO feedback ($\mathrm{W/m^2/K}$)		
		AIRS	IASI	Kernels
110-580	+3	-0.095 ± 0.062		0.0044 ± 0.046
595-635	+3	-0.022 ± 0.005		-0.023 ± 0.005
645-685	+5	0.013 ± 0.013	0.013 ± 0.011	0.026 ± 0.015
705-755	+3	-0.029 ± 0.005	-0.030 ± 0.005	-0.033 ± 0.005
805-995	+2	-0.095 ± 0.018	-0.079 ± 0.016	-0.10 ± 0.015
1015-1065	+3	-0.035 ± 0.007	-0.043 ± 0.007	-0.029 ± 0.006
1105-1205	+2	-0.045 ± 0.008	-0.042 ± 0.007	-0.048 ± 0.006

3.3 Atmospheric drivers of the radiative response

The ~~total spectral LW response is now separated into the~~ spectral fluxes of IASI and AIRS allowed us to study the total LW ENSO feedback associated with characteristic spectral regions and relate it to atmospheric and surface variables to which radiation is sensitive to. Now, we use the spectral radiative kernels to calculate the individual radiative contribution associated with changes in surface and atmospheric ~~Planck~~temperature, water vapor and ozone~~ENSO feedbacks using spectral radiative kernels. Their corresponding flux underwent to~~ , to investigate the origin of the ENSO signal in more depth. The corresponding surface and atmospheric Planck, water vapor and ozone ENSO feedbacks have been obtained by performing the same regression analysis ~~as of~~ that was performed on the IASI and AIRS observations. Results of the lagged regressions are plotted in Figure 4.

The Planck surface ENSO feedback (Figure 4, ~~third panel from the top)~~ panel a) is negative and contributes to the ~~total~~ TOA OLR only within the atmospheric windows, where the OLR is sensitive to the surface ~~. The associated slopes are positive and their maximum is centered at~~ temperature. It peaks at a lag equal to ~~+~~2 months ~~. The Planck atmospheric feedback~~ across the two spectral ranges ($\sim$ 800-1000 cm^{-1} and $\sim$ 1100-1200 cm^{-1}). A negative feedback is also associated to the Planck atmospheric effect (Figure 4, ~~fourth panel from the top) causes a positive response throughout all the spectral regions that peaks on average at lag +3 months, except between 645-700 cm^{-1}, where the slopes are negative and peak at 5-month lag, explaining the negative slopes observed in the two plots of Figure 3. The positive peak associated to~~ panel b) below about 600 cm^{-1}, between 700 - 1000 cm^{-1} and above 1100 cm^{-1}. Instead, the positive sign of the Planck atmospheric feedback between 645 - 700 cm^{-1} (Figure 4, panel b) explains the positive ENSO feedback that characterizes also IASI and AIRS observations at the center of the carbon dioxide band (Figure 3). In this spectral region the Planck atmospheric feedback ~~is located in the FIR spectral region, between ~ 400-600 cm^{-1}. Here the lag is of +~~peaks with a lag of 5 months, whereas over the remainder of the spectral range it peaks between 3 and 4 months lags. When the Planck atmospheric feedback is separated in a tropospheric and stratospheric contribution, ~~setting~~ with the tropical tropopause ~~layer~~ fixed at 100 hPa, it ~~is clear that the negative slopes come~~ becomes evident that the positive feedback originates from the stratospheric temperature change (Figure A2) and that the strong ~~positive slopes in~~ negative feedback within the FIR spectral region ~~are~~ comes from the troposphere (Figure A1), ~~particularly~~ with the largest contribution from the upper troposphere (600-150 hPa) (Figure A4). The Planck surface and atmospheric ~~feedback~~ feedbacks are both negative, enhancing the OLR emission. Water vapor changes, instead, ~~constitutes~~ constitute the main positive ~~feedback. Indeed, humidity changes cause negative regression slopes throughout the spectrum, meaning that a reduction in emissionof OLR takes place~~ENSO feedback, acting to dampen the OLR emission. The water vapor feedback peaks with a lag of 3 months at all wavenumbers. As for the Planck atmosphere, the ~~FIR is associated to the highest slopes, with most of the signal~~ strongest signal occurs in the FIR spectral region, with the majority of the contribution coming from the upper troposphere (Figure A4). ~~The water vapor feedback peaks with a lag of +3 months at all wavenumbers where the regression slopes are significant.~~

Given the strong ~~signal~~ ENSO feedback observed in correspondence of the ozone absorption band (Figure 3), we isolated the ozone contribution ~~as well. A small~~ to assess its specific impact. A negative feedback, peaking in the stratosphere (Figure A2), is found ~~around 1025 cm^{-1}. It enhances the OLR emission from +2 until +6 months~~ between about 1010 - 1065 cm^{-1}, with a pick at 4-months lag. At the same wavenumbers and lags there is also a smaller positive feedback associated to the stratospheric temperature (Figure A2), which, opposed to ozone, acts to reduce the OLR emission.

Finally, we reconstructed the total observed LW response summing the individual feedbacks calculated with kernels. The feedback sum is shown in Figure ~~3, second panel from the top,~~ 5, as a function of wavenumber and lag ~~. The individual slopes of water vapor, surface, temperature and ozone feedback, as well as their sum, is shown as afunction of wavenumbers for lag equal to +2 months in Figure 4, top panel . The major~~ (panel a) and wavenumber only for the 2-months lag (panel b), along with its components. The main features of the ~~observed~~ AIRS and IASI clear-sky OLR response (Figure 3) are present. The kernel regression analysis correctly reproduces the ~~positive slopes~~ negative feedback within the two atmospheric windows and ~~at~~ the wings of carbon dioxide absorption ~~band, and the negative slopes~~ bands, as well as the positive feedback at the center of it. ~~Their magnitude and time-lag is also well reproduced. However, there are two notable exceptions: the peak found in correspondence with the ozone absorption band~~Except for the magnitude of the latter, which is ~~underestimated by the kernel analysis, and the net signal in the FIR and MIR spectral region, which is positive and follows ENSOaccording to observations~~overestimated by the feedback sum with respect to AIRS (Table 2, third row), both the amplitude and time-lag are well reproduced (Table 2). The main discrepancy arises in the spectral regions below 600 cm^{-1} and above 1300 cm^{-1}: here AIRS fluxes indicate a negative feedback that peaks 3 months after ENSO, while the ~~opposite is suggested by the kernels sum~~kernels reconstruction indicates a contribution close to zero at that lag (Table 2, first row) and a positive feedback that anticipates the ENSO peak (Figure 5). A possible explanation ~~could be~~ lies in the fact that ERA5 profiles ~~are referred to~~ used in the kernel reconstruction represent all-sky ~~properties, that in the case of water vapor results in an~~ conditions. This leads to higher humidity content than ~~a~~ in clear-sky ~~profile~~ profiles, causing an overestimation of the ~~respective feedback , which masks the ozone signal and overcompensate the atmospheric temperature signal within the FIR and MIR regions. Within~~ associated water vapor feedback and leading to the complete compensation between the atmospheric temperature and water vapor signal below 600 cm^{-1} and above 1300 cm^{-1}

at positive lags. In the next section (Section 3.4), the spatial pattern of the OLR response to ENSO is examined, ~~this~~ which will help to ~~identify the regions associated to the previous biases~~trace the OLR response to specific regions of the tropical Pacific Ocean.

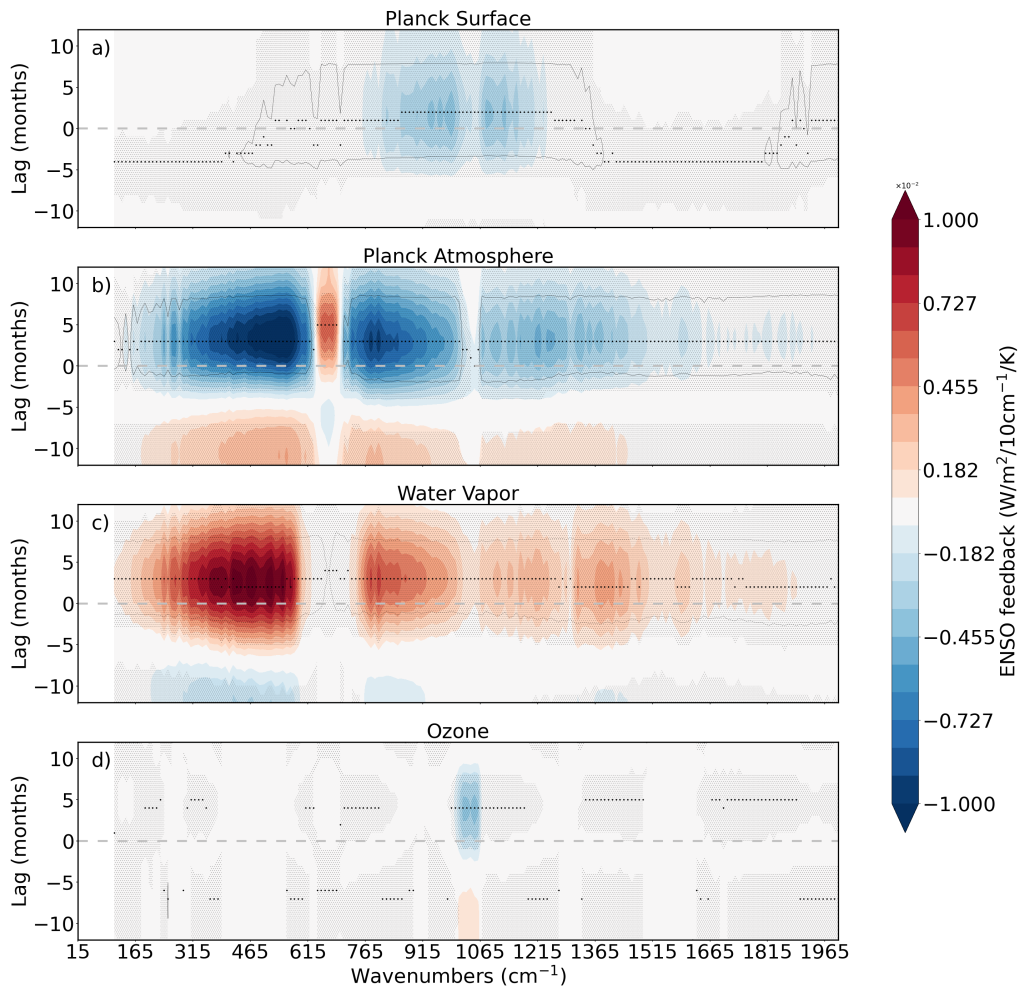

Figure 4. ~~Slopes of the lagged~~ Lagged regressions between ~~OLR anomalies and~~ the ~~Niño 3.4 index, but for radiative changes decomposed into Planck~~ tropical OLR anomaly driven by surface and atmospheric ~~, water vapor~~ temperature (panels a and ~~ozone ENSO feedback~~b), ~~and their sum. Slopes are reported as a function of wavenumber at a fixed lag of 2 months in the top panel (feedback sum in gray, Planck atmospheric feedback in red, Planck surface feedback in blue,~~ water vapor ~~feedback in cyan~~ (panel c) and ozone ~~feedback in purple~~(panel d) changes, and ~~as a function of wavenumber and lags in~~ the ~~panels below~~Niño 3.4 index. ~~Shades envelope the 95% confidence interval.~~ Thinner black dots mark 95% significance of the slopes, while thicker black dots mark the lag where the slope peaks at each wavenumber. As above, the sign of the OLR has been inverted (negative feedback = positive OLR anomaly).

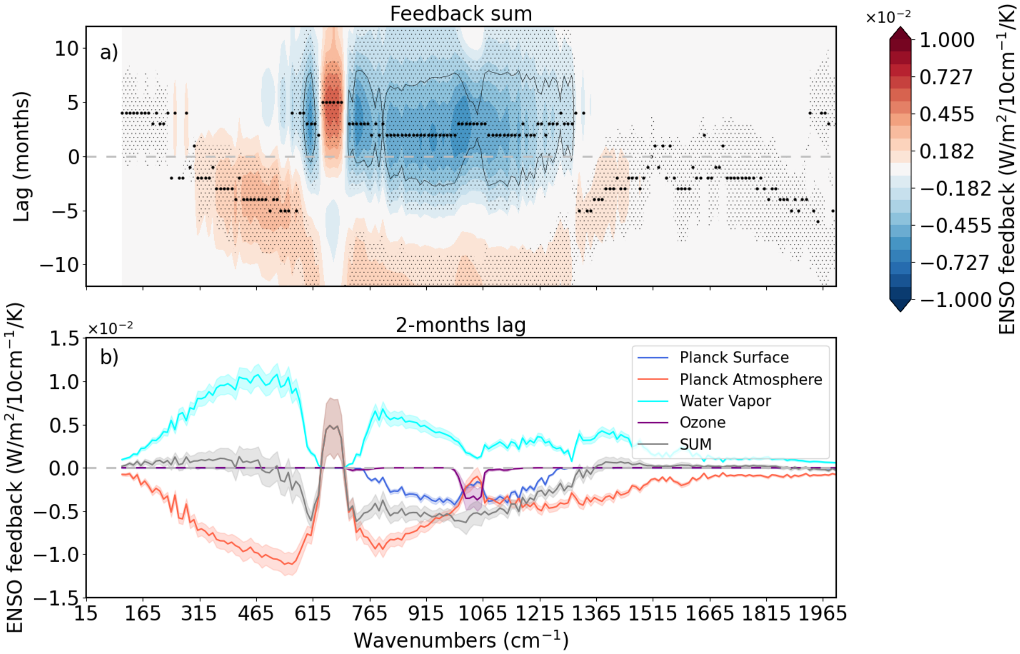

Figure 5. a) Total OLR ENSO feedback reconstructed from the sum of individual feedback reported in Figure 4. Thinner black dots mark 95% significance of the slopes, while thicker black dots mark the lag where the slope peaks at each wavenumber. b) Same ENSO Planck surface (blue), Planck atmospheric (red), water vapor (cyan) and ozone (purple) feedback as Figure 4, and feedback sum (gray) as panel a), but plotted for the 2-months lag. Shades envelope the 95% confidence interval. As above, the sign of the OLR has been inverted (negative feedback = positive OLR anomaly).

3.4 Spatial pattern of the longwave response to ENSO

We now examine the spatial pattern of the OLR response to ENSO across the tropics (30° S - 30° N)~~, to find the regions associated to the strong ozone response, and to the suspected bias due to the overestimation of the water vapor contribution.~~ .

~~Figure 6 shows the linear regressions between the OLR anomalies in individual spectral channels and the Niño 3.4 index at +2 months lag for every grid box within the considered area.~~ Starting from the top of Figure ~~4, the maps~~ 6, the ENSO feedback obtained for IASI~~(top), AIRS (mid)~~ , AIRS and the kernel ~~reconstructed signal (bottom) are~~ reconstruction is shown. The left column refers to the ~~channel at 905 cm^{-1}~~900-910 cm^{-1} interval, within the atmospheric window, ~~providing information on the~~ where OLR is sensitive to surface temperature, but also ~~on the effect of~~ to water vapor, that we want to assess and compare among ~~IASI, AIRS and the response reconstructed using spectral radiative kernels.~~

~~Slopes of the linear regressions at lag equal to +2 months between the tropical mean OLR anomalies, at two selected spectral channels, and the Niño 3.4 index, calculated at every grid box within the tropical zone (30°S-30°N). Starting from the~~

~~top, results for IASI, AIRS OLR and the feedbacks sum. On the left results at 905 cm^{-1}, on the right at 1025 cm^{-1}. Dots mark regions where the regressions reach the 95% significance level.~~

the observed and reconstructed signal. The right column corresponds to the ~~channel at 1025 cm^{-1},~~ 1020-1030 cm^{-1} interval, located within the ozone absorption band~~, sensitive mainly to the atmospheric temperature profile~~. Here, the OLR is mainly sensitive to surface temperature and ozone. ~~Here is where the highest positive response within the ozone absorption band - and the whole wavenumber range - is observed.~~ We want to recall that spectral kernels, as well as IASI and AIRS spectral fluxes, are expressed as the flux integrated over 10 cm^{-1} bands ($\mathrm{W/m^2/10cm^{-1}}$). Therefore, the wavenumbers selected represent the central value of the 10 cm^{-1} interval and not a single high-resolution channel.

At 905 ~~cm^{-1}, a dipole is observed~~ cm^{-1} the response, obtained from IASI and AIRS fluxes, shows a dipole within the tropical Pacific ocean, in phase with the SST pattern typical of El-Niño conditions. Indeed, ~~negative slopes characterize~~ a positive ENSO feedback characterizes the western part of the basin, while ~~positive values are~~ a negative value is found in the central and eastern ~~regions. Significant positive~~ parts of the basin. Significant negative contributions are also found over the north-east subtropical region and over the Maritime Continent. ~~The longwave~~

The OLR response at 1025 ~~cm^{-1}~~ cm^{-1} is characterized by ~~positive slopes~~ a positive feedback coming from the central and eastern part of the Pacific ocean. ~~Their~~ Its magnitude is highest within the Niño 3.4 region (marked by a black box in Figure 6), and decreases moving off the equator.

Overall, there is a good agreement in the pattern obtained ~~using~~ from IASI and AIRS products, although some minor differences can be observed. As ~~already~~ anticipated in Section 3.2, the ~~different temporal and spatial sampling between the two here becomes evident , as highlighted by the more scattered patterns of AIRS~~ impact of the clear-sky scene selection of AIRS observations is evident here. Specifically, AIRS shows a more scattered pattern with respect to IASI ~~. As mention before, the more conservative cloud filtering of AIRS can explain the slightly positive slopes within the atmospheric windows. In addition to that, the spatial pattern at~~ in the western and central tropical Pacific at 905 ~~cm^{-1} shows a less extent region of negative slopes in the west Pacific , constituting another reason for the higher slopes of AIRS . The response pattern is qualitatively well reproduced~~ cm^{-1}, where AIRS signal results lower in magnitude than IASI.

Although the feedback sum correctly reproduces the response pattern at 905 ~~cm^{-1} through the kernel reconstruction, although~~ cm^{-1}, the magnitude of the ~~negative slopes~~ positive feedback within the west Pacific is clearly overestimated. ~~Higher discrepancies are~~ A similar discrepancy is also obtained for the reconstructed response ~~pattern~~ at 1025 ~~cm^{-1}. Positive slopes characterize the eastern and central Pacific but their magnitude is smaller~~ cm^{-1}, where the signal in the central and eastern regions is smaller in magnitude than observations and ~~the~~ its peak is shifted eastward~~, with a region of negative slopes~~. The anomalous positive feedback can be attributed to the water vapor ENSO feedback. Indeed, it shows a positive signal in the western ~~Pacific, partly resembling the~~ and central part of the Tropical Pacific Ocean at both 905 ~~cm^{-1} pattern~~cm^{-1} and 1025 cm^{-1} (Figure 7). These differences consolidate our hypothesis of an overestimation of the water vapor feedback (Section 3.3), that would overcompensate the Planck contribution below 600 cm^{-1} and above 1300 cm^{-1} in the kernel reconstruction.

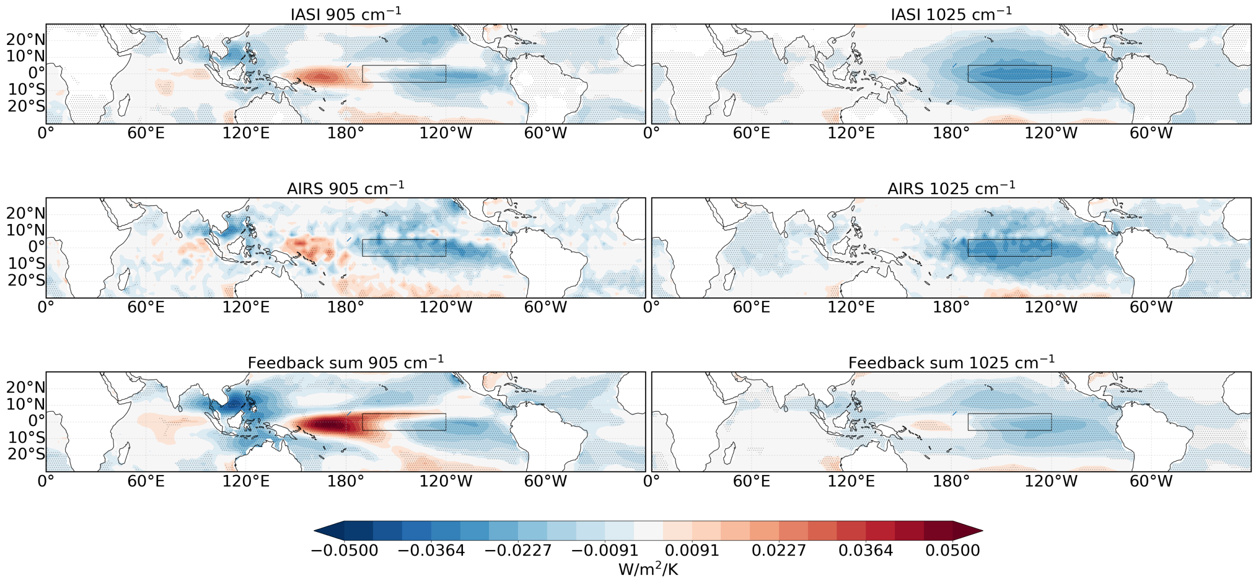

Figure 6. Spatial pattern of the total LW ENSO feedback of IASI (top maps), AIRS (central maps) and the kernels feedback sum (bottom maps), at 905 cm^{-1} (left maps) and 1025cm^{-1} (right maps), for a lag equal to two months. Black dots mark regions where the regressions reach the 95% significance level. The black rectangle highlights the Niño 3.4 region.

4 Discussion

The analysis reported in ~~section~~ Section 3 highlighted some key features of the LW radiative response to ENSO that help to understand and constrain the main processes behind the variability of the tropical radiative budget.

The main effect of ENSO on the climate system is the anomalous SST pattern across the tropical Pacific Ocean, accompanied by a shift of the Walker Circulation (WC) (Bjerknes, 1966). During the positive El-Niño phase warmer SST anomalies characterize the eastern and central part of the basin, while cooler SST are found in its western part. The WC is shifted eastward, with an increase in convective activity over the central Pacific and a decrease over the West Pacific warm pool. The negative ENSO phase, La-Niña, brings to the opposite conditions, accompanied by a strengthening of the Walker circulation.

~~In clear-sky conditions, the climate system responds to ENSO through an increase in OLR emission, that comes primarily from the tropospheric heating caused by~~ The period examined covers the years from January 2008 to December 2020, and it is characterized by two strong El-Niño events, as suggested by the Niño 3.4 index (Figure 1). The first peaked during the 2009-2010 winter and the ~~increase in surface temperature and by the increased latent heat release in the upper troposphere.~~ second during the 2015-2016 winter. During this period, two strong La-Niña events also occurred in 2008 and 2010. We analyzed the radiative response over the entire period, therefore taking into account the overall impact of successive El-Niño and La-Niña events on the tropical mean OLR anomaly.

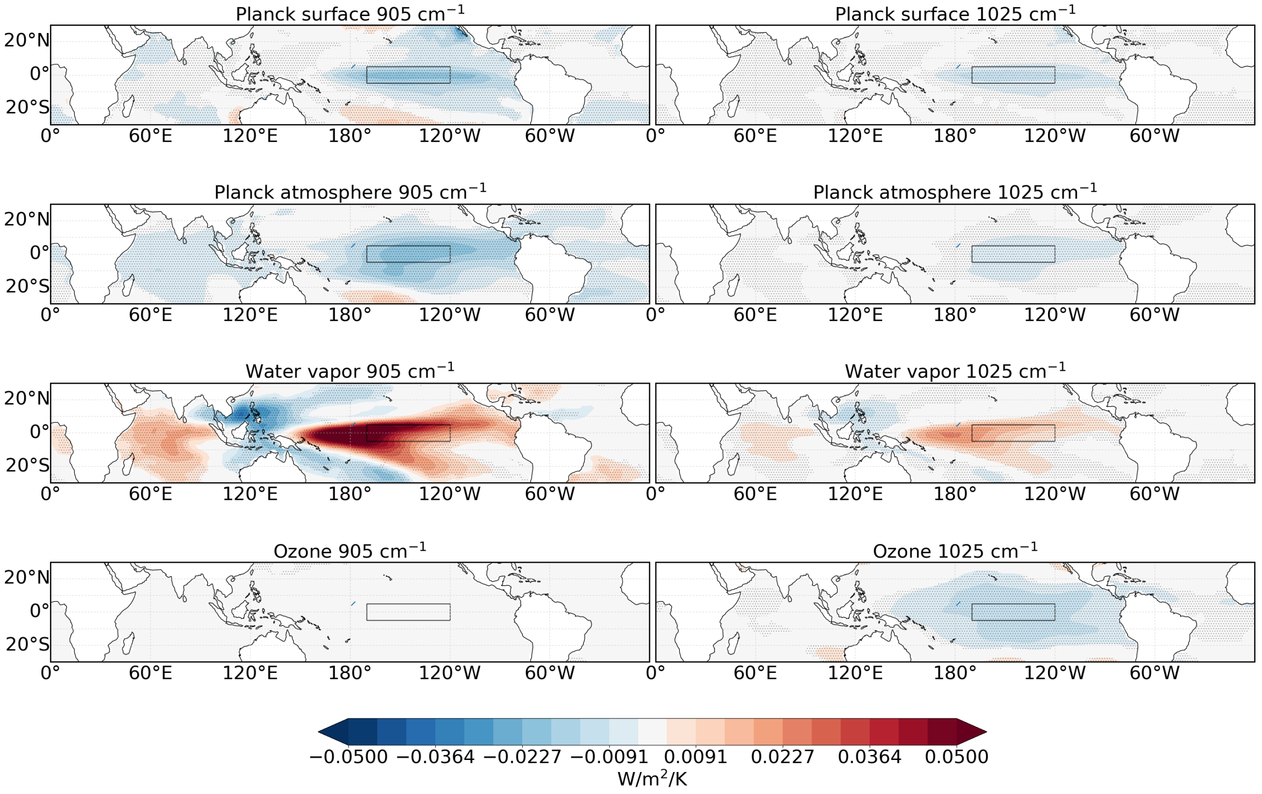

Figure 7. Spatial pattern of the Planck surface and atmosphere, water vapor and ozone ENSO feedback calculated using radiative kernels, at 905 cm^{-1} (left maps) and 1025cm^{-1} (right maps), for a lag equal to two months. Black dots mark regions where the regressions reach the 95% significance level. The black rectangle highlights the Niño 3.4 region.

In general agreement with Ceppi and Fueglistaler (2021), ~~this response is observed to reach its peak after and slowly decaying~~the clear-sky broadband OLR response suggests that ENSO activity during the time period considered resulted in an enhanced OLR emission at the TOA, whose peak lags ENSO by 2 months. The observed lag of the radiative response can be explained by the ~~SST pattern effect induced by ENSO, which causes warm SST anomalies to~~ fact that ENSO-induced SST anomalies are not constrained to the Niño 3.4 region but migrate across the tropical Pacific ocean from the east, at the beginning of an El-Niño event, to the west, where positive anomalies persist up to five months after ENSO peak (Ceppi and Fueglistaler, 2021).

~~Broadband lagged regressions show a peak of the~~ In this study, the combined use of spectrally resolved OLR measurements from the IASI and AIRS instruments, together with kernel analysis, allows the spectral response of OLR ~~response at 2-month lag. The spectral analysis shows that channels associated to this lag are the two atmospheric windows, whose radiance is mainly~~

~~sensitive to the surface temperature. Radiative kernels analysisfurther support that the delay of the clear-sky OLR response is likely driven by the Planck surface feedback~~to ENSO to be disentangled, showing how the lag varies across the different spectral ranges. Indeed, ~~it is the only one that peaks with a lag of 2 months.~~

~~However, a deeper insight is provided by spectrally-resolved OLR measurements. The strongest positive response is~~ the spectrally resolved fluxes show that channels associated to the ~~ozone absorption band and peaks at a 3-month lag . Others interesting features are the positive slopes at the wings of the carbon dioxide absorption band, where channels sensitive to tropospheric temperatures, which also peak at 3-month lag, and the negative slopes at the center of it, where radiation is~~ 2-month lag correspond to the atmospheric windows, whose radiance is mainly sensitive to the ~~stratospheric temperature. Their peak is the last at 5-month lag. With the aid of spectral radiative kernels, these features can be associated to the relevant physical processes that shape the OLR response to ENSO and its timing.~~

~~An increase in the time-lag of the OLR response is observed moving from the lower atmospheric layers to the higher. Specifically, the surface shows the earliest response at a lag of 2 months, followed by the troposphere, where the response peak lags ENSO of~~ surface temperature. The response in other spectral regions is further lagged, from 3 months ~~and the stratosphere, where a lag of~~ for regions sensitive to the upper troposphere to 5 months ~~is observed. As for regard the magnitude of the response, it is highest for channels~~ for the center of the CO_2 band, which is sensitive to the ~~troposphere, followed by channels sensitive to the stratosphere and the surface~~stratosphere, showing the impact of ENSO on the whole atmospheric column.

~~The tropospheric response instead, is shaped by two main feedbacks, the water vapor and the Planck atmosphere. The first informs on the radiative changes driven~~ Although it does not directly emerge from IASI and AIRS observations, the spectral kernel analysis also shows that within the atmospheric windows the water vapor feedback counteracts the Planck surface feedback. It is important to note that water vapor concentration is affected by humidity changes arising from the anomalous ~~WC during ENSO . An increase in water vapor is related to the ascending branch of the WC. It acts to~~ atmospheric circulation during ENSO Susskind et al. (2012). The effect of an increased water vapor concentration is to dampen the emission of OLR (positive feedback), absorbing most of the radiation emitted by the surface ~~resulting from~~ as a result of the increased SST. ~~As a consequence, the main cooling mechanisms is the emission related to the warming of the troposphere (Huang et al., 2021). The Planck atmosphere feedback is negative enhancing the OLR emission. Therefore, they act to~~ At the same time the negative Planck atmospheric feedback contributes to the OLR emission at these wavenumbers as the main cooling mechanisms of the system, as pointed out by (Huang et al., 2021).

The Planck atmospheric and water vapor feedback are dominant throughout the troposphere and counteract each other ~~and this is true also from a spectral point of view. We see that their lag is the same throughout all the spectrum~~throughout the entire spectrum (Figure 4, panels b and c). However, according to the overall negative LW response obtained from IASI and AIRS observations, the Planck atmospheric feedback dominates, leading to an overall increase in OLR emission across the entire spectrum. We observe that they generally peak at the same 3-month lag, except in the FIR region between 400 - 600 cm^{-1}, where the temperature peaks ~~one month later than water vapor . This evidences that the tropospheric cooling is maximum in~~

~~this spectral region and is associated to the temperature feedback coming from the upper troposphere.~~ at 3 months while the water vapor peaks at 2-months lag (Figure 3).

~~Moving to the stratosphere, the strong negative feedback within the ozone absorption band, together with the positive~~ When considering the ENSO-driven OLR response under clear-sky conditions, the main radiative feedbacks are those induced by temperature and water vapor changes. We obtain a value of -0.94 $\pm$ 0.05 $\mathrm{W/m^2/K}$ for the broadband temperature LW ENSO feedback (sum of the Planck surface and atmospheric feedback, integrated along the spectral dimension) at the three-months lag, which shows a fairly good agreement with that obtained by Kolly and Huang (2018) (see their Figure 3). While our broadband water vapor LW feedback, at the same time lag, is of 0.69 $\pm$ 0.07 $\mathrm{W/m^2/K}$, which is larger than that of Kolly and Huang (2018), which is around 0.5 $\mathrm{W/m^2/K}$ (see Figure 3 of Kolly and Huang (2018)). In addition to the different time period of the analysis, this can be explained both by the different set of radiative kernels used for the study, as well as the reanalysis product employed for the calculation of the radiative perturbations (ERA5 in this work and ERA-Interim in the work of Kolly and Huang (2018)). These results are also broadly consistent with the analysis carried out by (Raghuraman et al., 2019) (see their Table 3), although the different framework hampers a more quantitative comparison.

In addition, we found a significant negative feedback associated to ~~the stratospheric temperature, bear evidence of the ENSO~~ ozone changes. Together with the positive Planck atmospheric feedback observed at the center of the carbon dioxide absorption band, this reveals the ENSO-related stratospheric signal (Zeng and Pyle, 2005; Randel et al., 2009; Calvo et al., 2008; Manzini, 2009; Konopka et al., 2016; Manatsa and Mukwada, 2017; Garfinkel et al., 2018). According to (Domeisen et al., 2019), a reduction in ozone concentration near and above the tropopause is observed as a result of the anomalous upwelling during El-Niño, which cause an increase of ozone-poor air in the central and eastern tropical Pacific. This agrees with the spatial pattern reported in Figure ~~4~~7, which show that at 1025 $\mathrm{cm^{-1}}$ the ozone feedback ~~is located in regionsof increased convective activity~~characterizes these regions. Our analysis adds evidence to the attribution of IASI radiance trends in the ozone band in Whitburn et al. (2021) to ENSO-related ozone changes. In addition to composition changes, El-Niño also affects the stratospheric temperature. Specifically, an opposite response ~~respect to the troposphere is observed . If the troposphereexperiences an increase in temperature during El-Niño, the stratosphere cools.~~ is observed compared to the troposphere. The ENSO impact on stratospheric temperature is the result of the upward propagation of Rossby waves forced by El-Niño and the strengthening of the Brewer Dobson Circulation (BDC) (Domeisen et al., 2019). The stratospheric temperature decrease related to ENSO can explain the coherent decrease in TOA OLR emission observed at the center of the carbon dioxide absorption band ~~. Despite also involving~~ (Figure 3 and A2). Although a stratospheric signal ~~, the OLR decrease~~ is also involved, a decrease in the OLR is not observed in the ozone band, since the ozone concentration is also co-varying with ENSO near and above the tropopause, reversing the overall signal there. These findings confirm that the ENSO stratospheric signal plays an important role in shaping the LW radiative response peak.

5 Conclusions

In this work, we used spectrally resolved observation of the OLR to isolate and constrain the main processes controlling the inter-annual variability of the tropical energy budget. We focused on ENSO as the main driver of inter-annual radiative perturbations to the tropical OLR. ~~To the best of our knowledge, this is the first time that the radiative response to ENSO is analyzed using~~ Results further consolidate the potential of satellite-based spectrally-resolved measurements of the OLR ~~.~~ ~~Results show the potential of spectral OLR~~ to constrain the fast inter-annual feedbacks and isolate the processes driving them.

We recall here the main results of the study:

- The lagged regression analysis based on the spectrally-integrated tropical OLR from AIRS is largely consistent with CERES, with a slight delay of AIRS, likely due to the spatial sampling strategy used for the radiance to flux conversion. IASI and AIRS agree very well when integrated on the same spectral range, supporting the consistence among different data products.
- Further insight into the OLR response to ENSO is enabled by the spectral analysis:
  - The lag of the response is spectrally dependent, with channels sensitive to lower atmospheric layers peaking earlier than channels sensitive to the stratosphere.
  - The peak of the radiative response is found between ∼1000 - 1065 ~~cm^{-1}~~ cm^{-1} in correspondence with the ozone absorption band and follows ENSO by ~~3~~ three months.
- The spectral kernel analysis gives additional information on the processes driving the observed signal:
  - The Planck surface feedback (peaking at ~~2-months~~ two-months lag) and the Planck atmosphere feedback (~~3-months~~ three-months lag) are responsible for the negative LW feedback observed throughout the spectrum, that causes an increase in OLR following ENSO. The only positive feedback, which acts to decrease the OLR, is the water vapor feedback, that also peaks at ~~3-months~~ three-months lag.
  - The response at the center of the carbon dioxide absorption band together with the ozone is likely the result of ENSO induced changes to the stratospheric composition and temperature, which are important for the LW radiative response peak.
  - The sum of the Planck surface, atmosphere, water vapor and ozone feedback generally reproduces the observed signal, though with some differences. In particular, the ~~signal in the ozone absorption band is underestimated, and in the water vapor absorption bands in the FIR and MIR the water vapor~~ water vapor feedback perfectly balances the Planck atmosphere feedback, while the observations show that the temperature response prevails. These discrepancies may be caused by an over-estimation of the water vapor response due to ~~how the clear-sky fields of~~ the fact that the ERA5 ~~are obtained~~temperature/humidity fields refer to all-sky conditions.

In the FIR spectral region, both the water vapor and temperature ENSO feedbacks are higher, but to date we could only rely on simulated spectral fluxes at these wavenumbers. In this regard, an important contribution will be provided by the future

Far-infrared Outgoing Understanding and Monitoring (FORUM) mission, the selected Earth Explore-9 (EE-9) of the European Space Agency (ESA) (Palchetti et al., 2020), that will close this observational gap, allowing to assess the role of this critical region for the inter-annual and forced climate feedbacks.

This ~~study~~ work sets the basis for a ~~diagnostic~~ future investigation of ENSO-induced variability of the OLR ~~, based on spectrally resolved measurements, that~~ as simulated by climate models. The spectral dimension will allow to ~~better~~ disentangle the various processes contributing to ENSO OLR response ~~, avoiding compensation~~ avoiding compensating errors that may arise ~~by using the~~ from the use of broadband OLR. ~~We~~ In an upcoming study, we plan to apply this diagnostic to evaluate the climate models participating ~~to~~ in the Coupled Model ~~Inter-comparison Project phase~~ Intercomparison Project Phase 6 (CMIP6)~~in a upcoming work, which~~. This could improve our ~~insight on~~ understanding of how models reproduce the coupled atmosphere-ocean dynamics ~~driving the ENSO~~ that drive the El Niño–Southern Oscillation (ENSO) response.

Data availability. The CERES EBAF OLR fluxes are made available by NASA Langley Atmospheric Science Data Center (NASA/LARC/SD/ASDC), Distributed Active Archive Center (DAAC) via https://doi.org/10.5067/TERRA-AQUA/CERES/EBAF-TOA_L3B004.1 (NASA/LARC/SD/ASDC, 2019). AIRS Level 3 spectral fluxes are provided by Goddard Earth Sciences Data and Information Services Center (GES DISC) via https://doi.org/10.5067/5P7KQ31XI7XJ (Huang, 2020). IASI Level 3 spectral fluxes are provided by the Free University of Brussels/Laboratory for the study of Atmospheres, Environments, and Space Observations (ULB/LTMOS) via https://iasi-ft.eu/data-access/OLR/) (Whitburn, 2021a). ERA5 reanalysis products can be downloaded from Copernicus Climate Change Service (C3S) Climate Data Store (CDS) via https://doi.org/10.24381/cds.6860a573 (Hersbach et al., 2023a)

. Radiative spectral kernels are publicly available at https://doi.org/10.5281/zenodo.15487604.

Appendix A

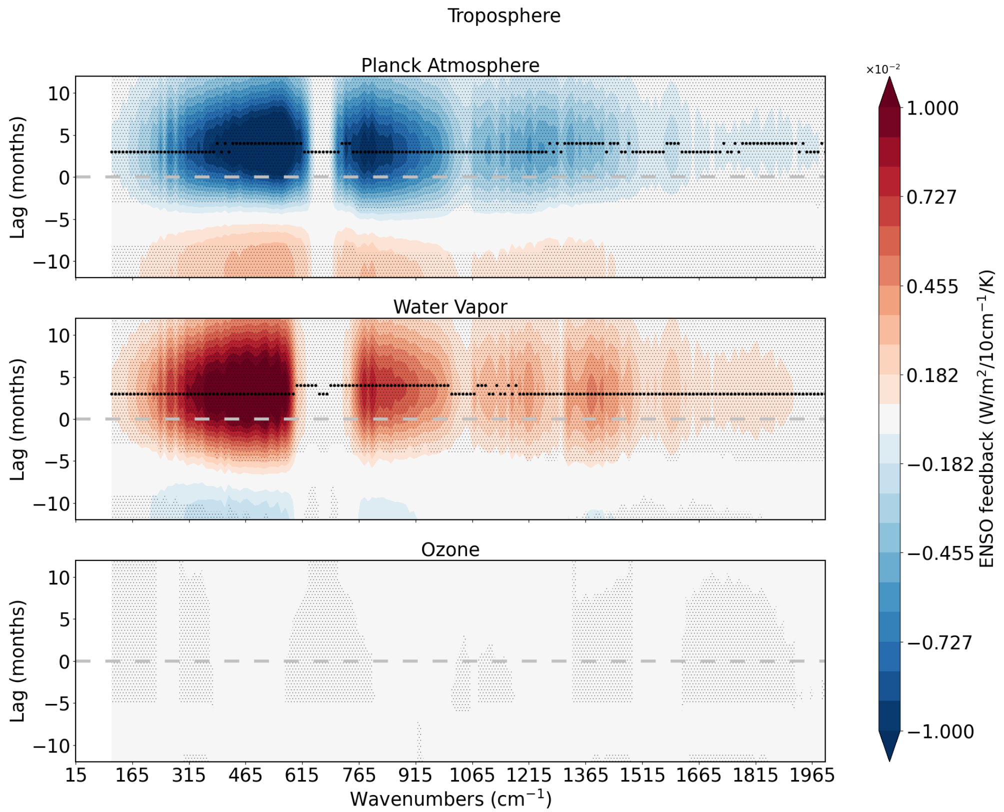

Figure A1. ~~Slopes of the lagged~~ Lagged regressions between ~~OLR anomalies and~~ the ~~Niño 3.4 index, but for~~ tropospheric ~~radiative changes decomposed into~~ OLR anomaly driven by atmospheric temperature, water vapor and ozone ~~ENSO feedback~~changes, and the Niño 3.4 index. The tropical tropopause is set at 100 ~~*hPa*~~hPa. Thinner black dots mark 95% significance of the slopes, while thicker black dots mark the lag where the slope peaks at each wavenumber.

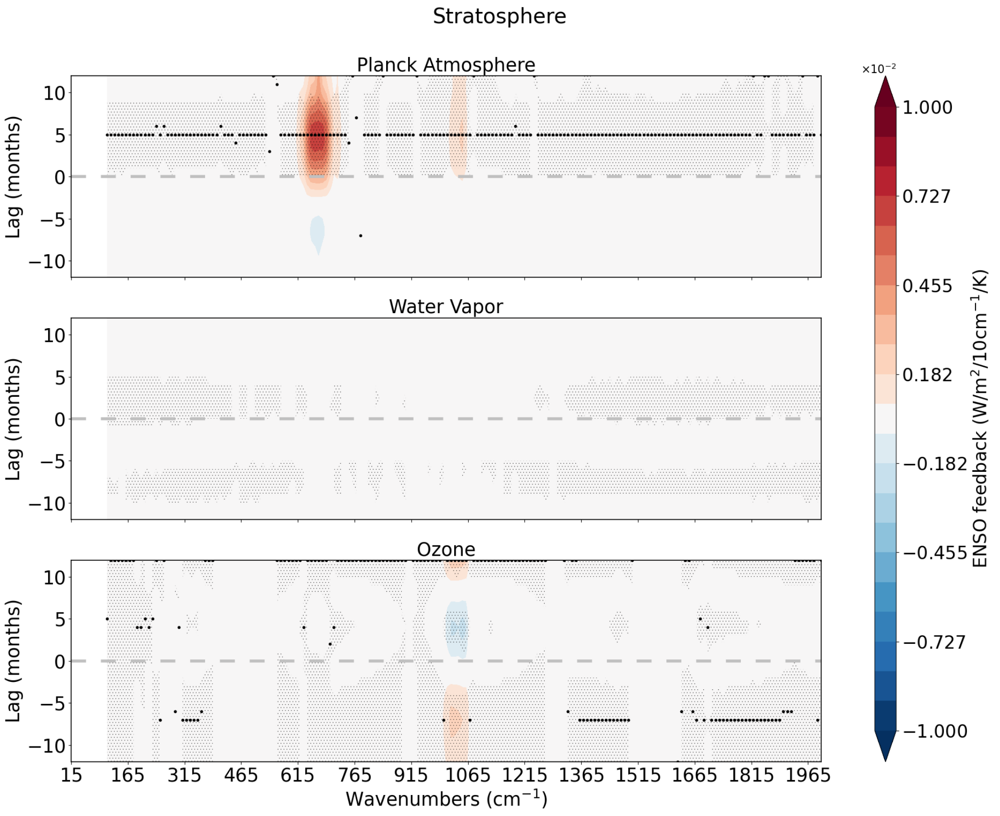

Figure A2. Same as Figure A1, but for radiative changes within the stratosphere (150 - 10 hPa).

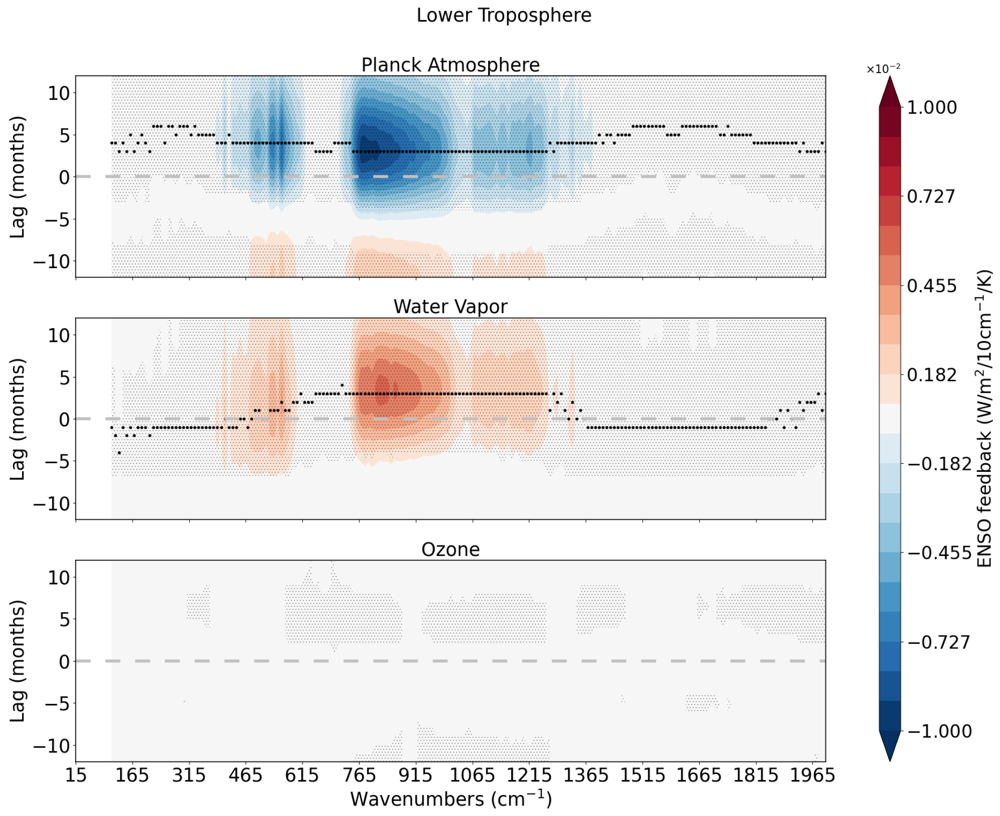

Figure A3. Same as Figure A1, but for radiative changes within the lower troposphere (~~1000-600 hPa~~1000 - 600 hPa).

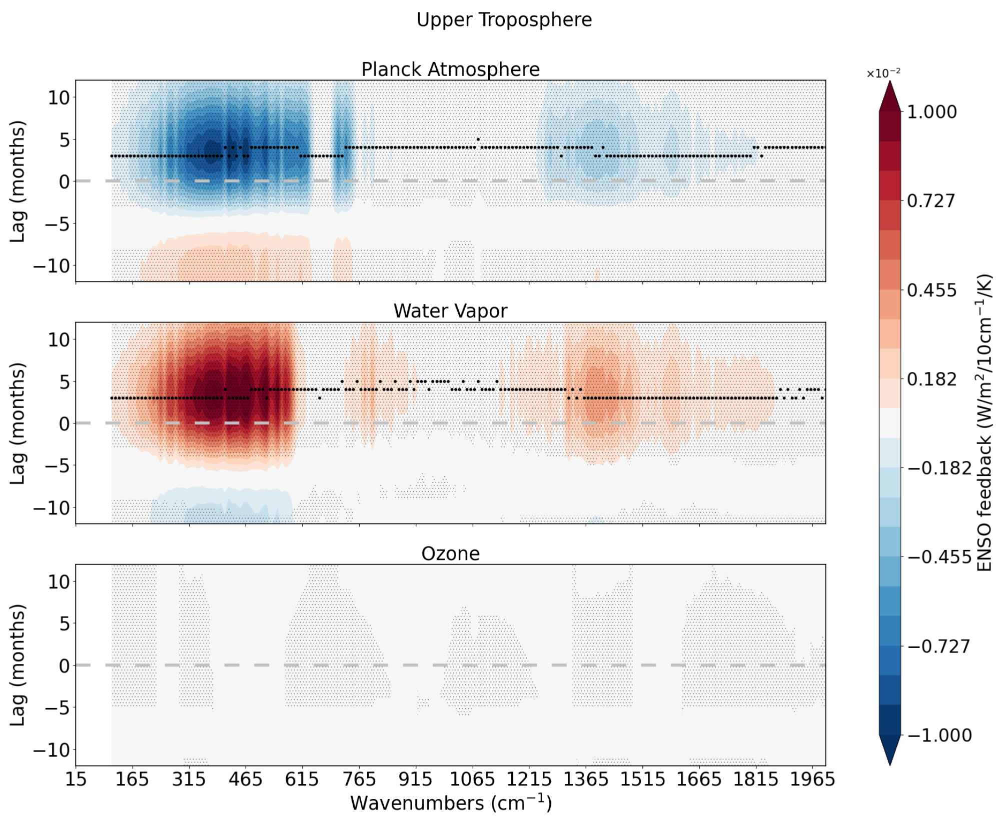

Figure A4. Same as Figure A1, but for radiative changes within the upper troposphere (~~600-150 hPa~~600 - 150 hPa).

Author contributions. "BM. D. and E. C. supervised the work. F. F. and S. DF. designed the experiments and M. T. carried out the formal analysis and wrote the manuscript with contributions from all co-authors."

Competing interests. All the authors declare that no competing interests are present.

Acknowledgements. This work has been supported by SERCO Italia s.p.a, who funded part of the PhD fellowship of M. Taddia, ~~within~~ during which this study has been developed. FF and SDF acknowledge support from the EMM - Earth-Moon-Mars project (PNRR, Mission 4, Component 2, Investment 3.1, Project IR000038, CUPC53C22000870006) and the MC-FORUM project (Meteo and Climate exploitation of FORUM) funded by the Italian Space Agency. The authors also ~~thanks~~ thank F. M. Palmeiro for the productive discussion on the ozone stratospheric dynamics and Professor X. Huang for the useful consultation which helped the set up of the beginning stages of this work. Finally, the authors would like to thank the three anonymous reviewers for their valuable comments.

References

Andrews, T., Gregory, J. M., and Webb, M. J.: The dependence of radiative forcing and feedback on evolving patterns of surface temperature change in climate models, Journal of Climate, 28, 1630–1648, 2015.

Andrews, T., Bodas-Salcedo, A., Gregory, J. M., Dong, Y., Armour, K. C., Paynter, D., Lin, P., Modak, A., Mauritsen, T., Cole, J. N., et al.: On the effect of historical SST patterns on radiative feedback, Journal of Geophysical Research: Atmospheres, 127, e2022JD036 675, 2022.

Armour, K. C., Proistosescu, C., Dong, Y., Hahn, L. C., Blanchard-Wrigglesworth, E., Pauling, A. G., Jnglin Wills, R. C., Andrews, T., Stuecker, M. F., Po-Chedley, S., et al.: Sea-surface temperature pattern effects have slowed global warming and biased warming-based constraints on climate sensitivity, Proceedings of the National Academy of Sciences, 121, e2312093 121, 2024.

Aumann, H. H., Chahine, M. T., Gautier, C., Goldberg, M. D., Kalnay, E., McMillin, L. M., Revercomb, H., Rosenkranz, P. W., Smith, W. L., Staelin, D. H., et al.: AIRS/AMSU/HSB on the Aqua mission: Design, science objectives, data products, and processing systems, IEEE Transactions on Geoscience and Remote Sensing, 41, 253–264, 2003.

Bjerknes, J.: A possible response of the atmospheric Hadley circulation to equatorial anomalies of ocean temperature, Tellus, 18, 820–829, 1966.

Brindley, H. and Bantges, R.: The spectral signature of recent climate change, Current Climate Change Reports, 2, 112–126, 2016.

Calvo, N., García-Herrera, R., and Garcia, R. R.: The ENSO signal in the stratosphere, Annals of the New York Academy of Sciences, 1146, 16–31, 2008.

Ceppi, P. and Fueglistaler, S.: The el niño–southern oscillation pattern effect, Geophysical Research Letters, 48, e2021GL095 261, 2021.

Clough, S. A., Iacono, M. J., and Moncet, J.-L.: Line-by-line calculations of atmospheric fluxes and cooling rates: Application to water vapor, Journal of Geophysical Research: Atmospheres, 97, 15 761–15 785, 1992.

Davis, L. L., Thompson, D. W., Rugenstein, M., and Birner, T.: Links between internal variability and forced climate feedbacks: The importance of patterns of temperature variability and change, Geophysical Research Letters, 51, e2024GL112 774, 2024.

Della Fera, S., Fabiano, F., Raspollini, P., Ridolfi, M., Cortesi, U., Barbara, F., and von Hardenberg, J.: On the use of Infrared Atmospheric Sounding Interferometer (IASI) spectrally resolved radiances to test the EC-Earth climate model (v3. 3.3) in clear-sky conditions, Geoscientific Model Development, 16, 1379–1394, 2023.

Della Fera, S., Fabiano, F., Raspollini, P., Ridolfi, M., von Hardenberg, J., and Cortesi, U.: Reproducing and Attributing IASI Radiance Trends with EC-Earth Climate Model Simulations, Journal of Climate, 38, 6943–6959, 2025.

Dessler, A., Zhang, Z., and Yang, P.: Water-vapor climate feedback inferred from climate fluctuations, 2003–2008, Geophysical Research Letters, 35, 2008.

Dessler, A. E.: A determination of the cloud feedback from climate variations over the past decade, Science, 330, 1523–1527, 2010.

Dessler, A. E.: Observations of climate feedbacks over 2000–10 and comparisons to climate models, Journal of Climate, 26, 333–342, 2013.

Domeisen, D. I., Garfinkel, C. I., and Butler, A. H.: The teleconnection of El Niño Southern Oscillation to the stratosphere, Reviews of Geophysics, 57, 5–47, 2019.

Garfinkel, C. I., Gordon, A., Oman, L. D., Li, F., Davis, S., and Pawson, S.: Nonlinear response of tropical lower-stratospheric temperature and water vapor to ENSO, Atmospheric chemistry and physics, 18, 4597–4615, 2018.

Hanke, T. and Proistosescu, C.: ENSO as an Emergent Constraint on the Pattern Effect, 2024.

Harries, J., Carli, B., Rizzi, R., Serio, C., Mlynczak, M., Palchetti, L., Maestri, T., Brindley, H., and Masiello, G.: The far-infrared Earth, Reviews of Geophysics, 46, 2008.

Hersbach, H., Bell, B., Berrisford, P., Biavati, G., Horányi, A., Muñoz Sabater, J., Nicolas, J., Peubey, C., Radu, R., Rozum, I., et al.: ERA5 monthly averaged data on pressure levels from 1940 to present [Data set], https://doi.org/10.24381/cds.6860a573, 2023a.

Hersbach, H., Bell, B., Berrisford, P., Biavati, G., Horányi, A., Muñoz Sabater, J., Nicolas, J., Peubey, C., Radu, R., Rozum, I., et al.: ERA5 monthly averaged data on pressure levels from 1940 to present, Copernicus Climate Change Service (C3S) Climate Data Store (CDS), 10, 2023b.

Huang, H., Huang, Y., and Hu, Y.: Quantifying the energetic feedbacks in ENSO, Climate Dynamics, 56, 139–153, 2021.

Huang, X.: Aqua AIRS Level 3 Spectral Outgoing Longwave Radiation (OLR) Monthly [Data set], https://doi.org/10.5067/5P7KQ31XI7XJ, 2020.

Huang, X. and Yung, Y. L.: Spatial and spectral variability of the outgoing thermal IR spectra from AIRS: A case study of July 2003, Journal of Geophysical Research: Atmospheres, 110, 2005.

Huang, X., Yang, W., Loeb, N. G., and Ramaswamy, V.: Spectrally resolved fluxes derived from collocated AIRS and CERES measurements and their application in model evaluation: Clear sky over the tropical oceans, Journal of Geophysical Research: Atmospheres, 113, 2008.

Huang, X., Chen, X., Soden, B. J., and Liu, X.: The spectral dimension of longwave feedback in the CMIP3 and CMIP5 experiments, Geophysical Research Letters, 41, 7830–7837, 2014.

Huang, X., JPL, A., et al.: Aqua AIRS level 3 spectral outgoing longwave radiation (OLR) monthly, NASA Goddard Earth Sciences Data and Information Services Center (DAAC) data set, p. 5P7KQ31XI7XJ, 2019.

Huang, Y. and Ramaswamy, V.: Observed and simulated seasonal co-variations of outgoing longwave radiation spectrum and surface temperature, Geophysical Research Letters, 35, 2008.

Huang, Y., Ramaswamy, V., Huang, X., Fu, Q., and Bardeen, C.: A strict test in climate modeling with spectrally resolved radiances: GCM simulation versus AIRS observations, Geophysical Research Letters, 34, 2007.

Kolly, A. and Huang, Y.: The radiative feedback during the ENSO cycle: Observations versus models, Journal of Geophysical Research: Atmospheres, 123, 9097–9108, 2018.

Konopka, P., Ploeger, F., Tao, M., and Riese, M.: Zonally resolved impact of ENSO on the stratospheric circulation and water vapor entry values, Journal of Geophysical Research: Atmospheres, 121, 11–486, 2016.

Leroy, S., Anderson, J., Dykema, J., and Goody, R.: Testing climate models using thermal infrared spectra, Journal of Climate, 21, 1863–1875, 2008.

Loeb, N. G., Kato, S., Su, W., Wong, T., Rose, F. G., Doelling, D. R., Norris, J. R., and Huang, X.: Advances in understanding top-of-atmosphere radiation variability from satellite observations, Surveys in geophysics, 33, 359–385, 2012.

Loeb, N. G., Rose, F. G., Kato, S., Rutan, D. A., Su, W., Wang, H., Doelling, D. R., Smith, W. L., and Gettelman, A.: Toward a consistent definition between satellite and model clear-sky radiative fluxes, Journal of Climate, 33, 61–75, 2020.

Manatsa, D. and Mukwada, G.: A connection from stratospheric ozone to El Niño-Southern Oscillation, Scientific Reports, 7, 5558, 2017.

Manzini, E.: ENSO and the stratosphere, Nature Geoscience, 2, 749–750, 2009.

Matricardi, M.: An assessment of the accuracy of the RTTOV fast radiative transfer model using IASI data, Atmospheric Chemistry and Physics, 9, 6899–6913, 2009.

McPhaden, M. J., Santoso, A., and Cai, W.: Introduction to El Niño Southern Oscillation in a changing climate, El Niño Southern Oscillation in a changing climate, pp. 1–19, 2020.

NASA/LARC/SD/ASDC: CERES Energy Balanced and Filled (EBAF) TOA Monthly means data in netCDF Edition4.1 [Data set], https://doi.org/10.5067/TERRA-AQUA/CERES/EBAF-TOA_L3B004.1, 2019.

Palchetti, L., Brindley, H., Bantges, R., Buehler, S., Camy-Peyret, C., Carli, B., Cortesi, U., Del Bianco, S., Di Natale, G., Dinelli, B., et al.: unique far-infrared satellite observations to better understand how Earth radiates energy to space, Bulletin of the American meteorological society, 101, E2030–E2046, 2020.

Planton, Y. Y., Guilyardi, E., Wittenberg, A. T., Lee, J., Gleckler, P. J., Bayr, T., McGregor, S., McPhaden, M. J., Power, S., Roehrig, R., et al.: Evaluating climate models with the CLIVAR 2020 ENSO metrics package, Bulletin of the American Meteorological Society, 102, E193–E217, 2021.

Raghuraman, S. P., Paynter, D., and Ramaswamy, V.: Quantifying the drivers of the clear sky greenhouse effect, 2000–2016, Journal of Geophysical Research: Atmospheres, 124, 11 354–11 371, 2019.

Randel, W. J., Garcia, R. R., Calvo, N., and Marsh, D.: ENSO influence on zonal mean temperature and ozone in the tropical lower stratosphere, Geophysical Research Letters, 36, 2009.

Roemer, F. E., Buehler, S. A., Brath, M., Kluft, L., and John, V. O.: Direct observation of Earth's spectral long-wave feedback parameter, Nature Geoscience, 16, 416–421, 2023.

Rugenstein, M., Van Loon, S., and Barnes, E. A.: Convolutional neural networks trained on internal variability predict forced response of TOA radiation by learning the pattern effect, Geophysical Research Letters, 52, e2024GL109 581, 2025.

Simeoni, D., Astruc, P., Miras, D., Alis, C., Andreis, O., Scheidel, D., Degrelle, C., Nicol, P., Bailly, B., Guiard, P., et al.: Design and development of IASI instrument, in: Infrared Spaceborne Remote Sensing XII, vol. 5543, pp. 208–219, Spie, 2004.

Stevens, B., Sherwood, S., Bony, S., and Webb, M.: Prospects for narrowing bounds on Earth's equilibrium climate sensitivity. Earth's Future, 4, 512–522, 2016.

Susskind, J., Molnar, G., Iredell, L., and Loeb, N. G.: Interannual variability of outgoing longwave radiation as observed by AIRS and CERES, Journal of Geophysical Research: Atmospheres, 117, 2012.

Trenberth, K. E.: The definition of el nino, Bulletin of the American Meteorological Society, 78, 2771–2778, 1997.

Uribe, A., Bender, F. A.-M., and Mauritsen, T.: Observed and CMIP6 modeled internal variability feedbacks and their relation to forced climate feedbacks, Geophysical Research Letters, 49, e2022GL100 075, 2022.

Uribe, A., Bender, F. A.-M., and Mauritsen, T.: Constraining net long-term climate feedback from satellite-observed internal variability possible by the mid-2030s, Atmospheric Chemistry and Physics, 24, 13 371–13 384, 2024.

Whitburn, S.: IASI-FT spectrally resolved Outgoing Longwave Radiation (from IASI/Metop-A, B and C) [Data set], https://doi.org/https://doi.org/10.21413/IASI-FT_METOPA_OLR_L3_ULB-LATMOS, 2021a.

Whitburn, S.: IASI-FT spectrally resolved Outgoing Longwave Radiation (from IASI/Metop-A, B and C), ULB/LATMOS data set, 2021b.

Whitburn, S., Clarisse, L., Bauduin, S., George, M., Hurtmans, D., Safieddine, S., Coheur, P. F., and Clerbaux, C.: Spectrally resolved fluxes from IASI data: Retrieval algorithm for clear-sky measurements, Journal of Climate, 33, 6971–6988, 2020.

Whitburn, S., Clarisse, L., Bouillon, M., Safieddine, S., George, M., Dewitte, S., De Longueville, H., Coheur, P.-F., and Clerbaux, C.: Trends in spectrally resolved outgoing longwave radiation from 10 years of satellite measurements, npj climate and atmospheric science, 4, 48, 2021.

Wielicki, B. A., Barkstrom, B. R., Harrison, E. F., Lee III, R. B., Smith, G. L., and Cooper, J. E.: Clouds and the Earth's Radiant Energy System (CERES): An earth observing system experiment, Bulletin of the American Meteorological Society, 77, 853–868, 1996.

Zelinka, M. D., Myers, T. A., McCoy, D. T., Po-Chedley, S., Caldwell, P. M., Ceppi, P., Klein, S. A., and Taylor, K. E.: Causes of higher climate sensitivity in CMIP6 models, Geophysical Research Letters, 47, e2019GL085 782, 2020.

Zeng, G. and Pyle, J. A.: Influence of El Nino Southern Oscillation on stratosphere/troposphere exchange and the global tropospheric ozone budget, Geophysical research letters, 32, 2005.